Regional tectonics of the Coso geothermal area along the intracontinental plate boundary in central eastern California: Three-dimensional V_p and V_p/V_s models, spatial-temporal seismicity patterns, and seismogenic deformation

Egill Hauksson[1] and Jeffrey Unruh[2]

Received 29 August 2006; revised 21 January 2007; accepted 27 February 2007; published 26 June 2007.

[1] We synthesize the tectonics of the southern Walker Lane belt and Coso Range in central eastern California using regional earthquake data. First, we invert for three-dimensional models of the V_p and V_p/V_s structure of the upper and middle crust. Using these models, we also determine three-dimensional V_s and Poisson's ratio models. The changes in seismic velocities across the region are small, except for low velocities in sedimentary basins and a ~2-km positive elevation of the basement velocities (V_p > 6 km/s) beneath the southern Sierra Nevada. Localized low-V_p and low-V_s zones beneath the central Coso Range image a geothermal reservoir at 0- to 3-km depth, as well as distinct low-velocity anomalies in the depth range of ~8 to ~12 km. Because the V_p/V_s has average crustal values within this broader zone, we interpret the anomaly to indicate a zone of few percent geothermal brines extending from 8- to 12-km depth. In addition, an embedded highly localized poorly resolved zone (possibly as small as 1 km^3) of slightly above average V_p/V_s and higher Poisson's ratio is a tentative suggestion of a small volume percent of magma present at depth of ~10 km. Second, we relocated the seismicity in the region using absolute traveltimes and differential traveltimes determined from waveform cross correlation. The relocated seismicity forms several spatially clustered lineaments along the southeast side of the Sierra Nevada and in the Indian Wells Valley and vicinity of the Coso geothermal field, which coincide with mapped late Quaternary faults in the region. The base of seismicity shallows from a regional depth of about ~11 to ~5 km beneath the central Coso Range, which we interpret as evidence for shallowing of the brittle-ductile transition zone beneath the geothermal field. In addition to abundant background seismicity, two large earthquake swarms, located 5 to 8 km to the west of Coso, occurred in April to May 1992 and May to June 2001. Two dual main shock-aftershock sequences also occurred as follows: the 1994 sequence near Ridgecrest and the later Coso earthquake sequence from late 1996 to early 1998, with the pairs of main shocks spaced 47 days and 16 months apart, respectively. Kinematic analysis of the focal mechanisms indicates that the crustal stress loading process varies across the region. The low-V_p anomaly, abundant seismicity, and crustal thinning provide quantitative evidence for the Coso region being an extensional releasing step over between two northwest-striking dextral faults: The Little Lake and Airport Lake fault zones to the south, and the Owens Valley fault to the north.

Citation: Hauksson, E., and J. Unruh (2007), Regional tectonics of the Coso geothermal area along the intracontinental plate boundary in central eastern California: Three-dimensional V_p and V_p/V_s models, spatial-temporal seismicity patterns, and seismogenic deformation, *J. Geophys. Res.*, *112*, B06309, doi:10.1029/2006JB004721.

1. Introduction

[2] The Sierran microplate in California is a plate fragment located within the broad zone of distributed deformation between the Pacific plate and stable North America. It includes the region east of the San Andreas Fault and north of the Garlock Fault and extends across most of eastern California south of Cape Mendocino [*Argus and Gordon*, 1991]. Northwest motion of the Sierran microplate with respect to stable North America

[1]Seismological Laboratory, Division of Geological and Planetary Sciences, California Institute of Technology, Pasadena, CA, USA.
[2]William Lettis & Assoc., Walnut Creek, CA, USA.

0148-0227/07/2006JB004721$09.00

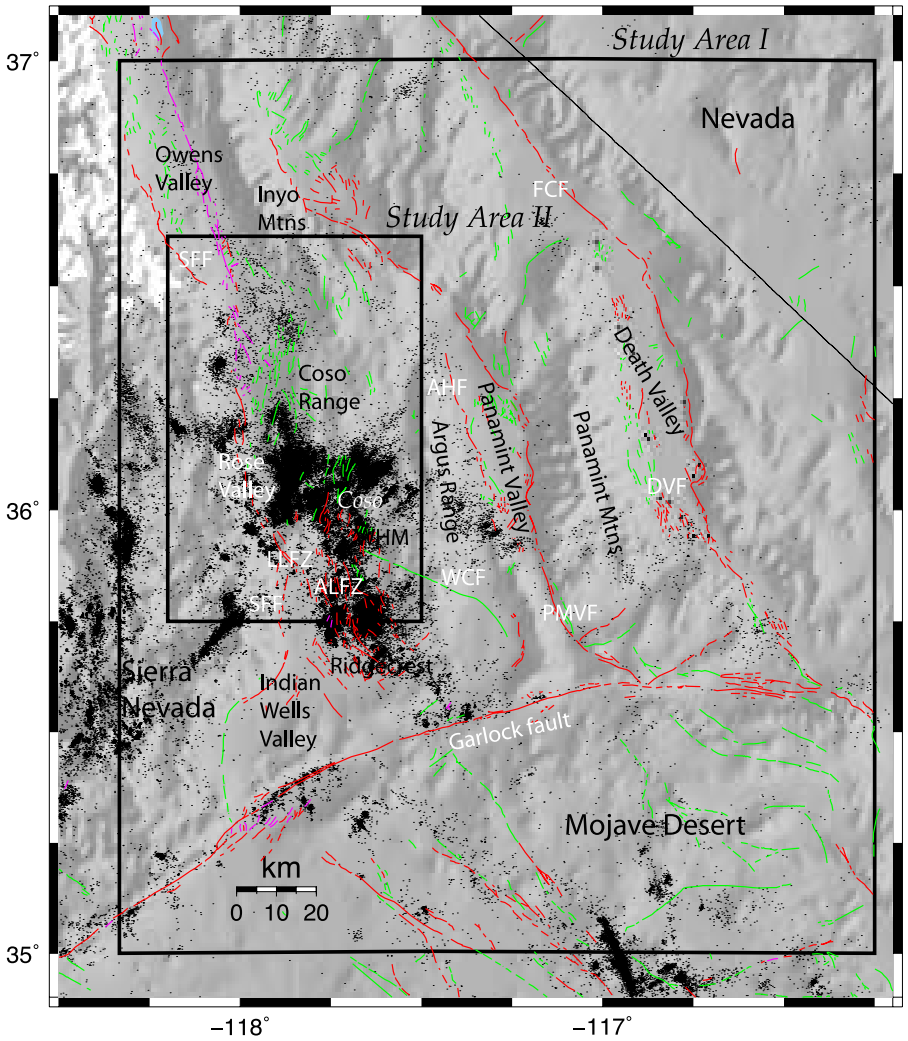

Figure 1. Relocated seismicity in southern California determined using three-dimensional velocity models [*Hauksson*, 2000]. The study area I, which includes seismicity used in the velocity inversion, is outlined by the large box. Study area II includes seismicity that was relocated using both absolute and double-difference traveltimes. AHF, Ash Hill fault; ALFZ, Airport Lake fault zone; DVF, Death Valley fault; FCF, Furnice Creek fault; LLFZ, Little Lake fault zone; PMVF, Panamint Valley fault; SFF, Sierran frontal fault; WCF, Wilson Canyon fault. Mapped faults from the work of *Jennings* [1994]; color coded with age as follows: red, Holocene; green, late Quaternary; magenta, early Quaternary.

is accommodated by transtensional dextral shear in the Walker Lane belt, a 100-km-wide zone of active deformation bordering the eastern Sierra Nevada [*McClusky et al.*, 2001; *Unruh et al.*, 2003]. Our study area, which includes the southernmost Walker Lane belt, extends across the southern Sierra Nevada and the southwestern most part of the Basin and Range Province. The study area is focused on the Coso geothermal field, a world-class geothermal resource in the central Coso Range (Figure 1).

[3] The Coso study area has a high rate of seismicity. The Southern California Seismic Network (SCSN) has recorded data from more than 87,000 earthquakes in the southern Sierra Nevada and the greater Indian Wells Valley-Ridgecrest-Coso Range region from 1981 to 2005 (shown as study area I in Figure 1). From 1981 to 2005, six events had magnitudes larger than 5, with the largest event of M5.8 occurring near Ridgecrest in September 1995 [*Hauksson et al.*, 1995], and the most recent M5.0 event occurring ~10 km northeast of Coso in March 1998. This high level of seismicity results from dextral transtension along the eastern margin of the Sierra Nevada microplate and potentially by other processes such as localized movement of crustal fluids in the Coso area.

[4] The geodetically determined rate of dextral shear associated with the Airport Lake-Owens Valley fault system (~5 mm/yr) is insufficient to explain the ongoing abundant microseismicity, and particularly that in the Coso geothermal field [*McClusky et al.*, 2001; *Wicks et al.*, 2001]. Although 23 years of seismicity exhibits a broad distribution extending from the southern Sierra in the west to the Panamint Mountains in the east, the seismicity is both spatially and temporally clustered on a local scale. Some of the individual seismicity clusters may be related to fluid flow, formation of

new faults, gravitationally driven extension associated with high Sierran topography, or variations in gravitational buoyancy forces that result from large horizontal gradients in potential energy associated with variations in topography and depth to the Moho. The concentration of seismicity near the Coso geothermal field may indicate a different causal stress field than the stress field driving the regional tectonic transtension. Alternatively, the seismicity patterns near Coso could be interpreted in the context of regionally uniform stress acting on laterally varying crustal rheology, which is reflected in the variable depth of the brittle-ductile transition (BDT) zone.

1.1. Previous Studies

[5] Numerous past studies have included both regional analysis of the southern Sierra Nevada and projects focused on the Coso geothermal resource. J. Unruh and E. Hauksson (Seismotectonics of an Evolving Intracontinental Plate Boundary, Eastern California, in review for *GSA Special Publication on the Walker Lane Belt*, 2007, hereinafter referred to as Unruh and Hauksson, in review, 2007) employed kinematic analysis of the regional SCSN earthquake data to infer that seismogenic extension of the southern Sierra Nevada is driven, at least in part, by gravitational buoyancy forces. To the east of the Sierran frontal fault, the regional patterns of seismogenic deformation are interpreted as distributed dextral shear, passing through the central Coso Range in a right-releasing step over between the Airport Lake fault zone to the south and Owens Valley fault to the north [*Unruh et al.*, 2002]. Numerous focused studies of the Coso area, published in 1980, included seismicity analysis [*Walter and Weaver*, 1980], teleseismic *P* wave imaging [*Reasenberg et al.*, 1980], tectonic interpretation [*Roquemore*, 1980], and past magmatic activity as well as state of stress [*Bacon et al.*, 1980]. All of these studies inferred transtensional tectonics and the presence of a magma chamber at a depth beneath Coso as the cause for the localized geothermal activity.

[6] Using teleseismic data, *Reasenberg et al.* [1980] found a maximum low-velocity contrast of 8% in the depth range of 10 to 17 km beneath the geothermal field and inferred the presence of a magma chamber. On the basis of petrological data, *Bacon et al.* [1980] inferred the presence of a N-S-aligned intrusive dike-melt system, and postulated a magma chamber at a depth of more than 8 km beneath the Coso area. Subsequently, using SCSN data, *Walck and Clayton* [1987] detected a low-V_p zone in the depth range of 5 to 10 km at the southern end of the Coso range but outside of the Coso geothermal area. In a study limited to the depth range from the surface to 10-km depth, *Walck* [1988] found a systematic decrease in V_p/V_s with depth beneath the Coso area but no obvious anomaly that could have been interpreted as a magma chamber. More recently, *Wilson et al.* [2003] used mostly vertical rays from teleseisms to calculate crustal receiver functions and infer that there was a low-velocity zone extending from depth of $\sim$5 km into the lower crust. On the basis of high V_p/V_s values, they inferred a rhyolitic magma chamber with an $\sim$5% melt in the 5- to 17-km depth range.

[7] Previous studies of the Coso area have suggested a relationship between the geothermal activity and seismicity. *Walter and Weaver* [1980] found a similar depth distribution of seismicity as presented in this study and inferred a north-south compression from focal mechanisms. Using local Coso seismicity data, *Lees* [2002] described the three-dimensional geophysical properties of the geothermal field and provided newer, detailed geophysical imaging of the uppermost 3 km than of the crust. Most recently, *Monastero et al.* [2005] interpreted data from the Coso region and proposed a model for the evolution of the Coso region as a nascent, actively evolving metamorphic core complex. They used evidence from seismicity, gravity, petrology, and strong asthenospheric signature in geothermal fluids to argue for crustal thinning and accompanying elevation of the brittle-ductile transition to 5-km depth beneath the geothermal field.

[8] The geology of the Coso area is dominated by the quartz-rich granites of the Sierra Nevada as compiled in a detailed geology map by *Walker et al.* [2002]. *Wilson et al.* [2003] also provided a summary geology map of the region showing the distribution of sediments and the Neogene volcanics in the Coso Range. The granitic rocks are intruded with small volumes of igneous rocks ranging from basalt to rhyolite in composition. The quartz-rich granites are expected to have slightly below average values of both V_p and the V_p/V_s [*Christensen*, 1996]. In contrast, if the igneous rocks have significant spatial extent, the crustal velocity models would be expected to have above average values of both V_p and V_p/V_s [*Hauksson*, 2000]. The possible presence of basaltic to rhyolitic magma chambers could be imaged as low V_p and high to low V_p/V_s or Poisson's ratio, depending on the silica content of the magma, crack aspect ratios, and volume percent of magma [*Nakajima et al.*, 2001].

1.2. Goals of This Study

[9] In this study, we analyze regional SCSN earthquake data to determine three-dimensional V_p, V_s, V_p/V_s, and Poisson's models and associate improved earthquake hypocenters and focal mechanisms in the study region with late Quaternary faults. We also compare the velocity models and the relocated seismicity to facilitate joint interpretation of the two data sets. In particular, we are looking for spatial changes in the character of the velocity structure and the seismicity, possibly associated with late Quaternary faults such as the Sierra frontal fault or other geological structures. To synthesize the regional tectonics of the Coso Range, we also determine the seismogenic deformation field by inverting groups of focal mechanisms for reduced incremental strain tensors [*Twiss et al.*, 1993].

[10] Within the Coso-Ridgecrest area, we seek to characterize the size, shape, and amplitudes of anomalies in the velocity structure at depth as well as their location relative to the geothermal field and the locus of Pleistocene rhyolitic volcanism in the Coso Range. In particular, we are interested in imaging from the surface down to depths of 15 km and to compare our results to other studies such as *Wilson et al.* [2003] and *Monastero et al.* [2005]. This study complements the work of *Unruh et al.* [2002] in the Coso area and Unruh and Hauksson (in review, 2007) in the southern Sierra Nevada, who used the focal mechanisms from this

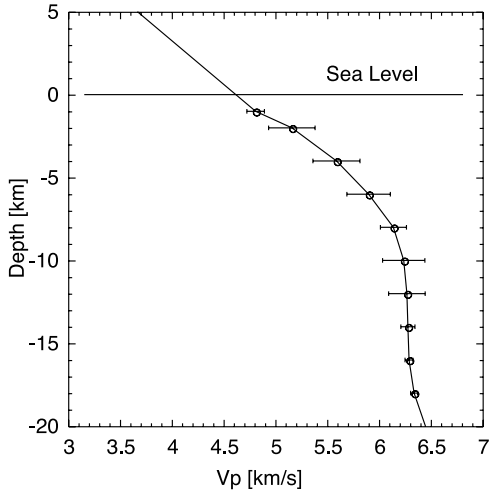

Figure 2. The starting one-dimensional V_p model with error bars for the southern Sierra and the Coso regions.

study for detailed kinematic analysis of the seismogenic deformation.

2. Methods and Data

2.1. Determining Three-Dimensional V_p, V_s, V_p/V_s, and Poisson's Ratio Models

[11] To invert for the regional three-dimensional velocity models, we applied the method of *Thurber* [1993] and the detailed approach described in the work of *Hauksson* [2000], which consists of a three-step process. First, we selected the one-dimensional starting model from the average model of *Hauksson* [2000] and inverted for a one-dimensional model that provides the best overall average fit to the traveltime residuals of the data set (Figure 2).

[12] We selected an even distribution of 3387 earthquakes because they provide relatively uniform coverage across the region and have ample raypaths to constrain the model (Figure 5). To obtain even ray coverage across the region, we used the velocity model grid and selected events with the greatest number of phase picks within 3 km of each

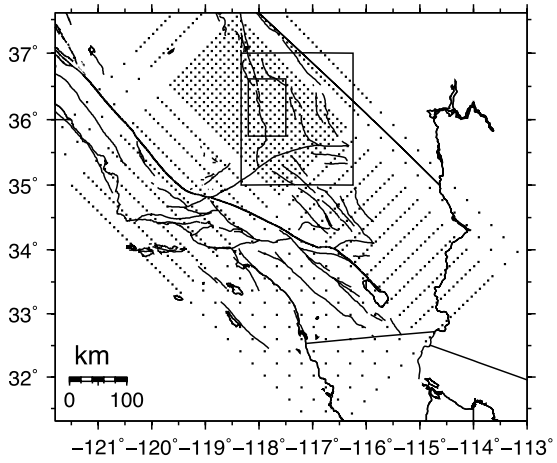

Figure 3. The three-dimensional velocity grid with 10-km grid spacing and the outlines of the study areas I and II. This is a modified grid from the work of *Hauksson* [2000].

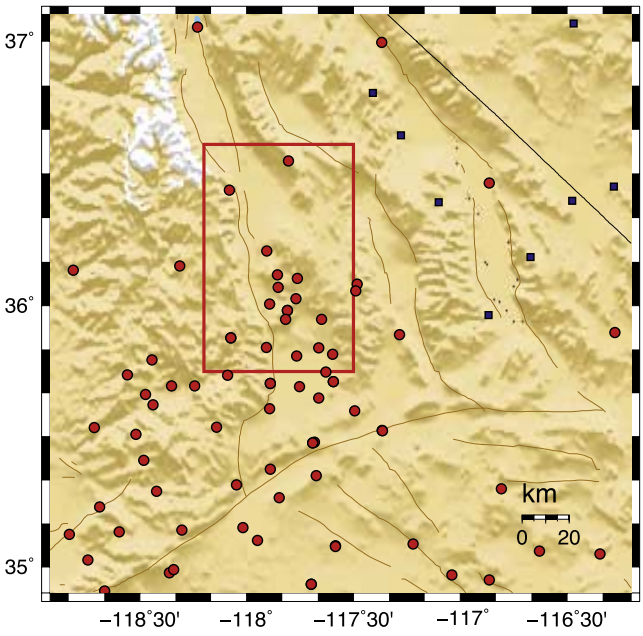

Figure 4. Map of study area I showing the Southern California Seismic Network (SCSN) stations as filled circles and the seismic stations operated by University of Nevada, Reno as squares. Outline of the study area II is included. Data recorded at these seismic stations that are located within the model region were used in the velocity model inversions.

node, including all the depth layers. The depth range is from 1.0 to 18 km, and the magnitude range is from M1.8 to M5.7. On average, 22 *P* picks and 4 *S* picks are available for each of these events.

[13] We gridded the one-dimensional model into a uniform three-dimensional model (Figure 3). The horizontal gridding is modified from *Hauksson* [2000] but the new vertical gridding has the layers spaced 2 km apart down to 18-km depth, to provide improved depth constraints for possible anomalies. The damping was selected to minimize the root-mean square traveltime residuals while also minimizing the model length [see also *Hauksson*, 2000]. The seismic stations in the study region, which are more numerous in the southwest quadrant of the model, are shown in Figure 4. Additional data recorded by other SCSN stations were also included in this study. Third, we inverted for the spatially varying three-dimensional model. We selected the lowest possible damping for the three-dimensional model to reach the appropriate balance between simultaneously minimizing the traveltime residuals and the model length. The V_p and V_p/V_s models include 75,000 *P* and 12,600 *S* picks from the 3387 earthquakes (Figure 5). The final three-dimensional velocity model was used to relocate the seismicity in the area from 1981 through January 2005.

[14] We applied the three-dimensional V_p and V_p/V_s velocity models following the formula from the work of *Christensen* [1996] to determine the Poisson's ratio,

$$\sigma = \frac{1}{2}\left[1 - \frac{1}{(V_p/V_s)^2 - 1}\right], \qquad (1)$$

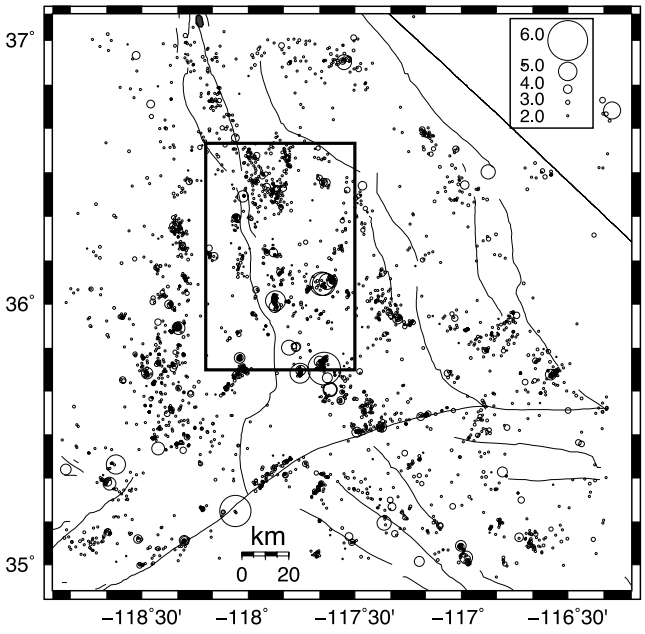

Figure 5. The seismicity in study area I that was used to select a set of phase picks for the inversion of the new three-dimensional velocity models (Figures 6 and 7). Outline of the study area II is also included.

of the upper and middle crust of the study region. Similarly, we determined the V_s model from the ratio of V_p and V_p/V_s.

2.2. Earthquake Relocations

[15] The Southern California Seismic Network (SCSN), jointly operated by Caltech and the US Geological Survey, recorded the waveforms and provided the absolute *P* and *S* arrival time data used in this study. This study includes data from more than 87,000 earthquakes that have occurred in the study region from 1981 to January 2005 (study area II in Figure 1).

[16] We applied waveform cross correlation to the seismograms of all the recorded earthquakes in study area II (Figure 1), using the approach presented by *Hauksson and Shearer* [2005]. Waveforms recorded by the SCSN were first extracted from the Southern California Earthquake Data Center (SCEDC) data center in 50 s windows that included both *P* and *S* waves. The traces were then resampled to a uniform 100 Hz sample rate and band-pass filtered to between 1 and 10 Hz. We divided the area into six processing regions with approximately 10,000 earthquakes within each region. Next, we applied time domain waveform cross correlation for *P* and *S* waves between each event and 100 neighboring events that were identified from the catalog based on the three-dimensional velocity model of *Hauksson* [2000]. We determined differential times from the peaks in the cross-correlation functions and used a spline interpolation method to achieve a nominal timing precision of 0.001 s.

[17] These differential times, together with existing *P* and *S* phase picks, were input to the double-difference program of *Waldhauser and Ellsworth* [2000] to further refine the hypocenters in the study area. The absolute location accuracy on average ranges from 0.5 to 2.0 km horizontally and 1.0 to 4 km vertically. The relative hypocentral errors are at least factor of 10 to 20 smaller when the differential times are included in the double-difference method [*Waldhauser and Ellsworth*, 2000].

2.3. Calculation of Focal Mechanisms

[18] We used the method of *Hardebeck and Shearer* [2002] to determine 12,484 first-motion focal mechanisms for events that had 12 or more first motions reported within study area II (Figure 1). We used the hypocenters determined with the double-difference method as starting locations. The method performs a grid search to find a set of all mechanisms for each event that are acceptable, using an expected polarity error rate and the range of allowed hypocenters and velocity models. Thus the method takes into account possible errors in the earthquake location, velocity model, and polarity observations. It also removes outliers, which may be identified during the grid search, and the remaining solutions are averaged to find the best focal mechanism for each earthquake.

[19] To facilitate plotting of the focal mechanisms, we used the rake angle to characterize earthquakes as normal ($-90° \pm 45°$), thrust ($90° \pm 45°$), or strike-slip events (all other rake values). The errors in strike, dip, and rake range depend on the number of available first motions and their distribution with azimuth and take-off angle. On the average, the rake may have uncertainties of $\sim 20°$ and thus lead to a few events not being plotted in the right figure.

3. Results: Regional Three-Dimensional Models

[20] The three-dimensional V_p and V_p/V_s models extend from the interior of the southern Sierra Nevada on the west to the California state border on the east, and from Owens Valley on the north across the Coso-Ridgecrest area to about 50 km south of the Garlock Fault (Figures 6 and 7). All the models are displayed in horizontal depth sections at depths below sea level from 1.0 to 14 km; however, depth layers at 16-, 18-, and 31-km depth are not shown because of limited resolution. The station coverage in the southern Sierra Nevada and Coso regions is relatively dense, but to the north and east of the Coso Range, the coverage is sparse. Similarly, the background seismicity tapers off to the north and east. Consequently, the models are well resolved except along the north and east edges.

[21] We use the derivative weighted sum (DWS) as a metric of the information density provided by the ray coverage. The DWS measures the weighted ray density in the neighborhood of every node. Numerous past studies [e.g., *Thurber*, 1993; *Hauksson*, 2000] have shown that the DWS values track well the diagonal elements of the resolution matrix and possible smearing as indicated by the more formal spread function. In Figures 6 and 7, the model areas that have DWS values less than 300 for V_p and 150 for V_p/V_s, which inherently have less dense ray coverage, are not shown. To provide additional details about resolution of the models, the diagonal elements of the resolution matrix are presented in the Appendix.

3.1. The Three-Dimensional V_p Model

[22] The regional variations in V_p are small but significant (Figure 6). All of the depth slices show an increase in velocity with depth, superimposed on similar distributions

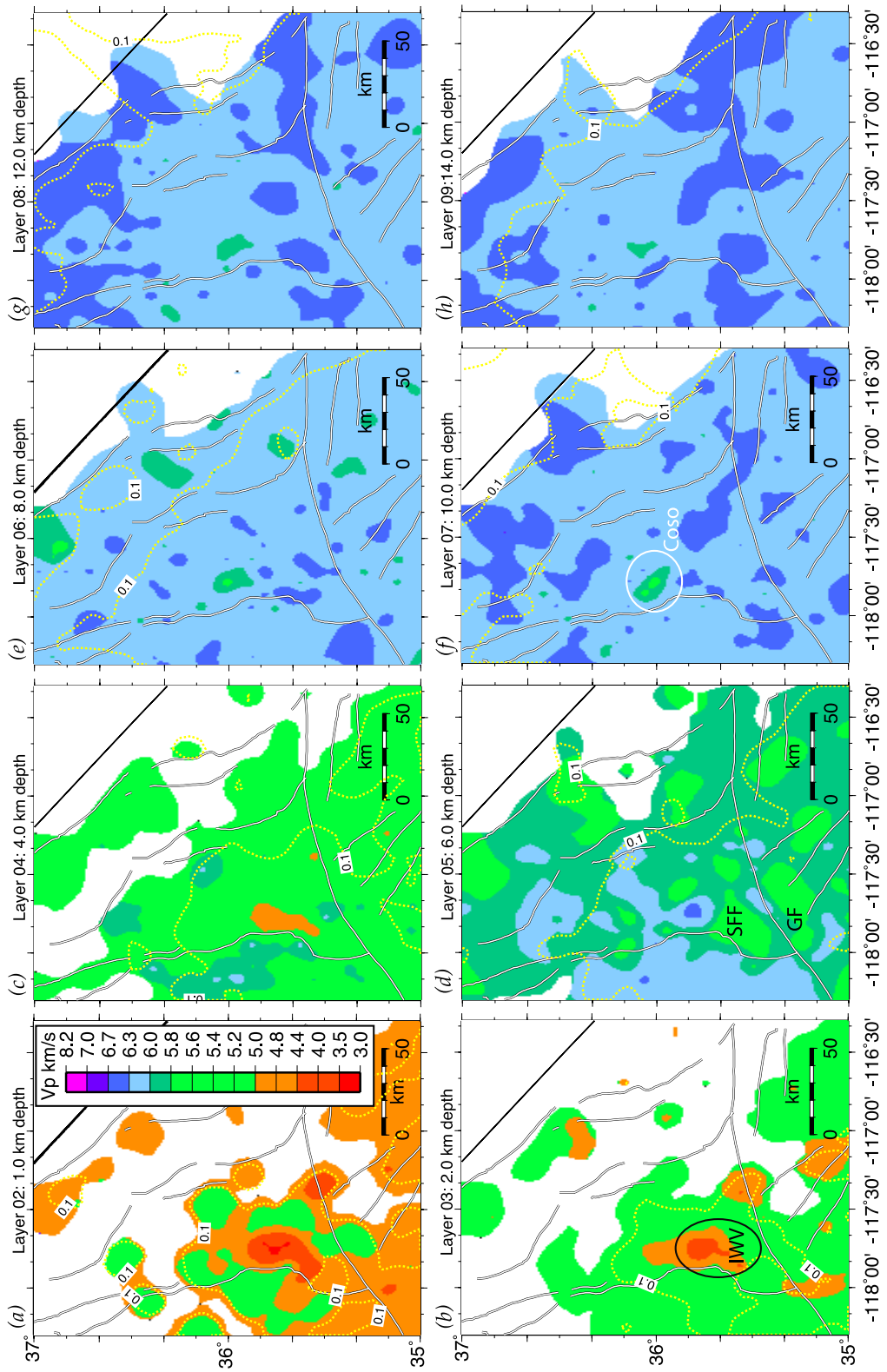

Figure 6. The three-dimensional V_p model in the southern Sierra Nevada and Coso-Ridgecrest area is shown in map view at eight different grid layer depths at (a) 1-, (b) 2-, (c) 4-, (d) 6-, (e) 8-, (f) 10-, (g) 12-, and (h) 14-km depths. The depths of the grid layers were chosen to capture the large gradient in the near surface velocities. The unresolved parts of the model are not shown where the ray density or the derivative weighted sum (DWS) is less than 300. Major faults are plotted in white. Dashed yellow curves are the 0.1 contour of the diagonal element of the resolution matrix; for other contours, see Figure A1. Also, see Figure 1 for names of major geographical features and faults. GF, Garlock Fault; IWV, Indian Wells Valley; SFF, Sierran frontal fault.

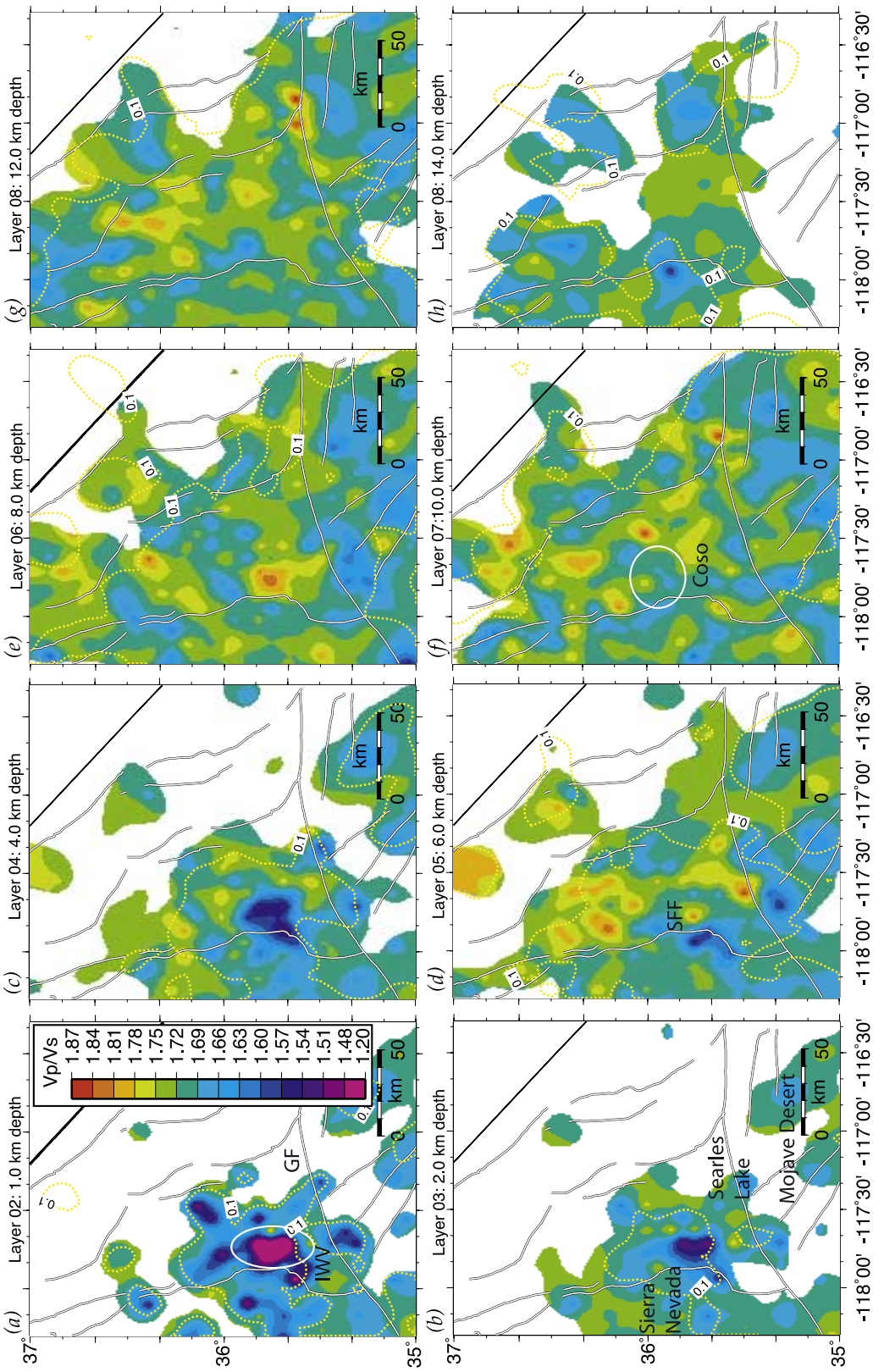

Figure 7. The three-dimensional V_p/V_s model shown in depth slices at (a) 1-, (b) 2-, (c) 4-, (d) 6-, (e) 8-, (f) 10-, (g) 12-, and (h) 14-km depth. The unresolved parts of the model are not shown where the ray density or the derivative weighted sum (DWS) is less than 150. Major faults are plotted in white. Dashed yellow curves are the 0.1 contour of the diagonal element of the resolution matrix; for other contours, see Figure A2. See Figure 1 for major geographical and fault names. GF, Garlock Fault; IWV, Indian Wells Valley; SFF, Sierran frontal fault.

of irregular regions of slightly higher or lower velocities with scale lengths ranging from 15 to 30 km.

[23] The V_p increases abruptly from about 3 to 4 km/s in the near surface to ~6.0 km/s or greater values, dominating at depths of 8 km. In the depth range of 1 to 4 km, the regional variations in V_p correspond to sedimentary basins and bedrock outcrops in the study region as mapped by *Walker et al.* [2002]. There is a prominent low-V_p anomaly associated with Indian Wells Valley, which is best expressed in the upper 2 km and, in some areas, is imaged to 4-km depth. Generally, these images are consistent with independent data, such as borehole data that reveal about 2 km of Tertiary sedimentary strata above Mesozoic crystalline rocks [*Monastero et al.*, 2002], and analyses of gravity data that indicate that the basin may be as deep as 3 km or more in the northwestern part of the valley [*Black et al.*, 2002]. To the south and east in the study region, other V_p anomalies associated with late Cenozoic basins such as Searles Lake are shallower and only imaged in the near surface.

[24] The 6-km V_p depth section (Figure 6) shows that the middle-crust basement, as defined by the V_p of 6 km/s, is imaged at ~2-km shallower depth beneath all of the southern Sierra Nevada than areas to the east. Scattered middle-crust basement highs are also present beneath the Coso and the southern Inyo Ranges to the north of the Coso geothermal area. The eastern edge of the elevated middle-crust basement beneath the Sierra is coincident with the Sierran frontal fault. This variation in depth to higher V_p could be related to extensional faulting and associated decrease in average elevation of crustal blocks in the southeastern region of the basin and range. Alternatively, the positive relief on the middle-crust basement in the southern Sierra may be due, at least in part, to late Cenozoic surface uplift of the range.

[25] The V_p models are fairly homogeneous at depths greater than 8 km, with spatially restricted, low-amplitude anomalies of alternating higher and lower V_p. The high-amplitude, low-V_p anomaly that coincides with the Coso geothermal field extends across several depth layers for V_p, from depths of 8 to 12 km. Other low-V_p anomalies are more localized and only occur in a very limited depth range and thus are difficult to interpret or associate with geological structures. The deepest part of the model from 10 to 14 km shows increasing presence of high V_p of 6.3 to 6.7 km/s, which are the middle to lower crustal rocks.

3.2. Three-Dimensional V_p/V_s Model

[26] The spatial pattern of V_p/V_s variations is similar to that exhibited by the V_p model, although V_p/V_s responds to lithology, anisotropy, and crustal fluids differently than V_p (Figure 7). Nearly all of the near-surface V_p/V_s anomalies are regions with lower values of V_p/V_s of 1.25 to 1.6, which could be related to sediments with high silica content and/or the presence of open cracks [*Christensen*, 1996; *Walsh*, 1965]. The most prominent V_p/V_s low coincides with Indian Wells Valley, extending to depths of 3 km. Such low V_p and low V_p/V_s values for sediments are rare [*Brocher*, 2005] and suggest unusual geological conditions. Such geological conditions that may be created by high silica content and textural characteristics of the sediment such as poor sorting and an open framework structure exist in the Indian Wells Valley [*Monastero et al.*, 2002].

[27] In the depth range from 6 to 14 km, the spatial variations in V_p/V_s are small and there is no obvious correspondence between the low-V_p/V_s anomalies and the geological structure of the region. In particular, at 10-km depth beneath the Coso geothermal field, the variations in V_p/V_s are small in geographical extent (less than ~1 km) and have only moderately large amplitudes.

3.3. Regional Spatial-Temporal Seismicity Patterns

[28] To improve the spatial and temporal resolution of seismicity patterns, we relocated the 1981 to 2005 seismicity in the greater Ridgecrest-Coso region, which is shown as study area I in Figure 1. These relocated hypocenters are distributed from the Garlock Fault in the south to the Owens Valley lake in the north, and they form two major clusters as follows: one to the south and centered around Ridgecrest, and the second centered around Coso (Figure 8). In addition, there are several small clusters in the eastern Sierra Nevada, such as the Scodie lineament [*Bawden et al.*, 1999]. Many of these small clusters form linear trends striking either N35°E to N40°E, or N20°W, and thus, in some cases, form pairs of conjugate faulting. However, there are no obvious seismicity clusters along the Sierran frontal fault. One of the most prominent features in the spatial distribution of seismicity is the abrupt transition north of Coso from a very seismically active region to an aseismic region. *Walter and Weaver* [1980] suggested that this transition resulted from different crustal rocks to the north, which is supported by the three-dimensional V_p/V_s model presented here that exhibits elevated values to the northwest of Coso.

[29] The Ridgecrest-area seismicity primarily consists of two sequences that occurred in 1980 to 1982 and in 1995. The 1981–1982 sequence migrated from north to south over a distance of 12 km. Some ground cracking associated with the M_L4.9 Indian Wells Valley earthquake sequence was reported by *Roquemore and Zellmer* [1983] along the Airport Lake fault zone, suggesting shallow focal depths. The M_L5.4 August 1995 earthquake exhibited normal faulting, while the M_L5.8 September 1995 earthquake exhibited strike-slip faulting [*Hauksson et al.*, 1995]. These

Figure 8. Relocated seismicity determined using three-dimensional velocity models shown in (a) map view and (b) time-distance plot, latitude versus 1981 to 2005. In both map view and space-time plot, the 1981–2005 is shown as black circles and the $M \geq 4.0$ earthquakes are shown as red stars. The Landers and Coso induced seismicity trends are marked with arrows. Red star filled with yellow, Coso Hot Springs; Red filled star, Red Hill Volcano; Green star, Ridgecrest; ALFZ, Airport Lake fault zone; GF, Garlock Fault; LLFZ, Little Lake fault zone; SFF, Sierran frontal fault; WCF, Wilson Canyon fault, WHM, White Horse Mesa. County boundaries are also shown as black lines. (395), California Highway 395 (blue lines). Mapped faults from the work of *Jennings* [1994]: red, Holocene; green, late Quaternary; magenta, early Quaternary; black, pre-Quaternary.

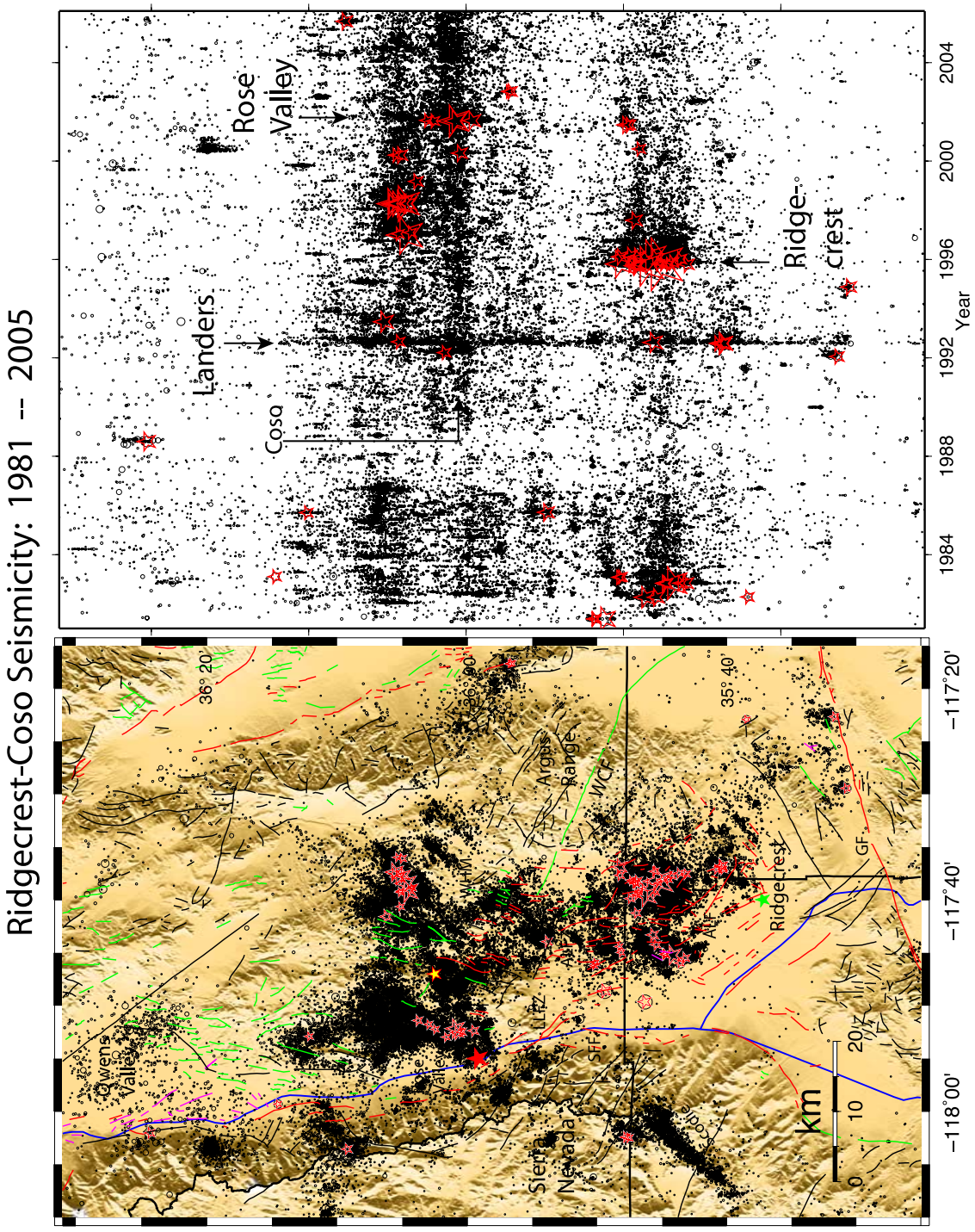
Ridgecrest-Coso Seismicity: 1981 -- 2005
Landers
Rose
Valley
Coso
Ridge-
Crest
1984
1988
1992
1996
2000
2004
Year
36° 20'
35° 40'
−118°00'
−117°40'
−117°20'
Owens
Valley
Sierra
Nevada
Argus
Range
WCF
Ridgecrest
GF
SFF
LLF
km
0
10
20

Figure 8

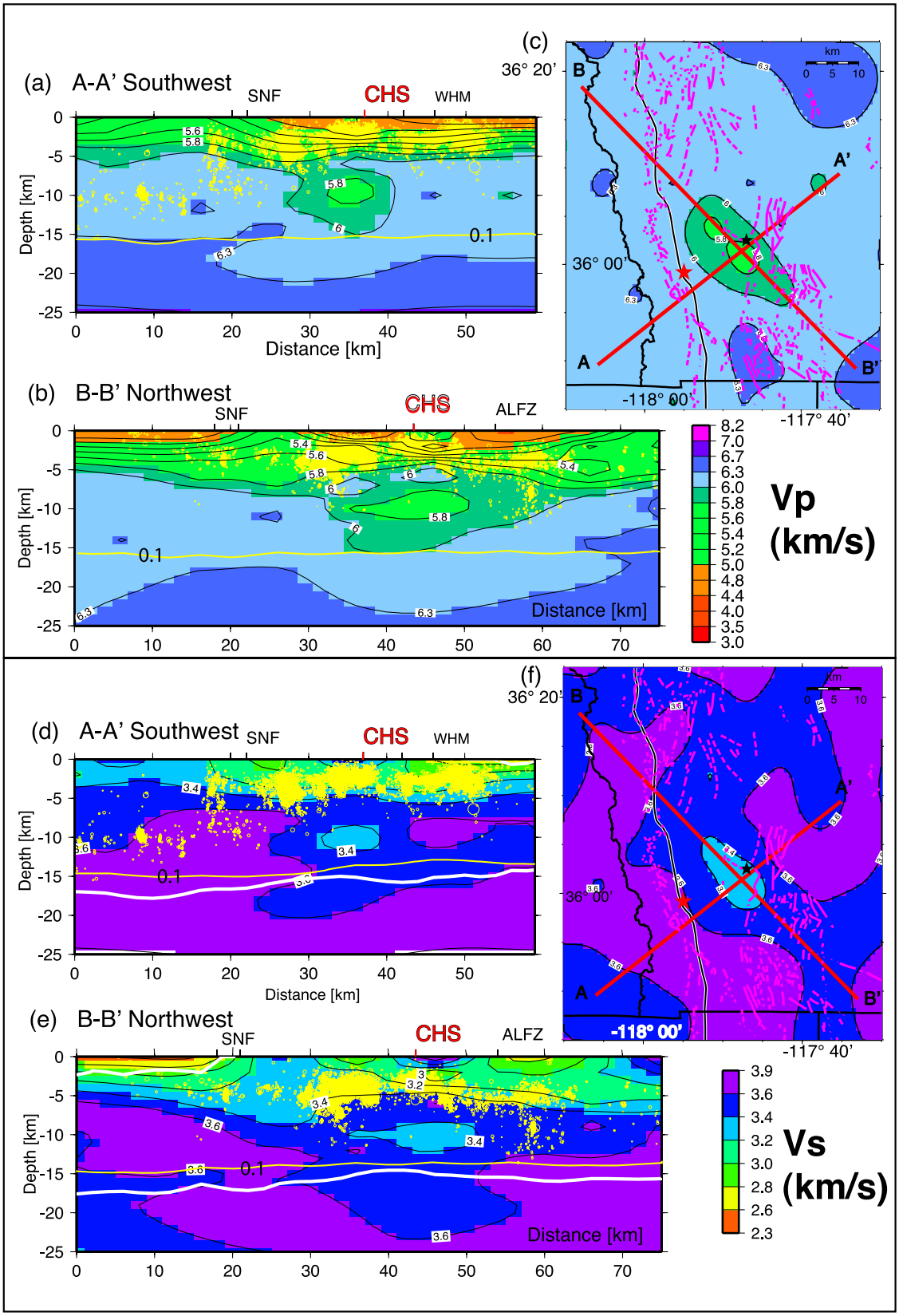
(a) A-A' Southwest
SNF
CHS
WHM
Depth [km]
Distance [km]
(b) B-B' Northwest
SNF
CHS
ALFZ
Distance [km]
(c)
36° 20'
36° 00'
-118° 00'
-117° 40'
A
A'
B
B'
km
0 5 10
Vp
(km/s)
8.2
7.0
6.7
6.3
6.0
5.8
5.6
5.4
5.2
5.0
4.8
4.4
4.0
3.5
3.0
(d) A-A' Southwest
SNF
CHS
WHM
Depth [km]
Distance [km]
(e) B-B' Northwest
SNF
CHS
ALFZ
Distance [km]
(f)
36° 20'
36° 00'
-118° 00'
-117° 40'
A
A'
B
B'
km
0 5 10
Vs
(km/s)
3.9
3.6
3.4
3.2
3.0
2.8
2.6
2.3
0.1

Figure 9

two following main shocks that were followed by more than 4500 aftershocks and were located within 3-km distance of each other occurred at different focal depths: The first main shock was shallow at 4 km, and the second was at 7-km depth. Similar variations in faulting style, from normal to strike-slip, with depth were also reported beneath Wild Horse Mesa, to the east of Coso, by *Unruh et al.* [2002].

[30] The time-space patterns of the Ridgecrest-Coso seismicity include both naturally occurring and triggered seismicity (Figure 8b). In the early to mid-1980s the seismicity consisted of fairly uniform background with numerous short-lived swarms. In the late 1980s the induced seismicity at Coso began developing and became more distinct through the 1990s and 2000s. *Feng and Lees* [1998] first pointed out that the Coso microseismicity has increased since the start of fluid injection related to exploitation of geothermal energy. They suggested that the induced seismicity resulted from shear fracturing caused by fluid injection and subsequent circulation along major existing fractures. In mid-1992 the M_w7.3 Landers earthquake triggered a large swarm extending across the whole study region. This triggering of small earthquakes suggests that the region is close to being critically stressed and ready to produce small- to moderate-sized earthquakes. The 1999 M_w7.1 Hector Mine earthquake did not cause such widespread triggering, possibly because of rupture directivity to the south and less ground shaking.

4. Interpretation of Three-Dimensional Models and Refined Seismicity Patterns

[31] The three-dimensional models, refined seismicity patterns, and focal mechanisms provide a consistent picture of the transtensional tectonics of the Coso area. The two cross sections, ($A - A$') from the southwest and ($B - B$') from the northwest, provide detailed images of the V_p, V_s, V_p/V_s, and Poisson's models in the Coso area (Figures 9 and 10). *Wagner et al.* [2005] suggested that, if V_s was determined from a joint V_p and V_p/V_s inversion, the V_s model could be contaminated by the V_p model. A spike test discussed in the Appendix, showed that the contamination is less than ~1% for our data set. Below we provide further insight into the tectonics through joint interpretation of the three-dimensional models and seismicity data.

4.1. V_p and V_s Models

[32] The V_p and V_s models beneath the Coso geothermal field exhibit sharply increasing vertical gradients in V_p and V_s down to depths of 5 km (Figure 9). Previously, *Wu and Lees* [1999] found similar vertical gradients in near-surface V_p and V_s within the Coso geothermal area. Below 6-km depth, the V_p gradually decreases, forming a prominent low-V_p anomaly (5.8 km/s) in the depth range of 8 to 12 km. This anomaly is roughly elliptical in map view, with the major axis to the northwest and minor axis to the southwest. Furthermore, the V_p anomaly also has two zones of lower V_p, one centered beneath Coso, while the other is located ~8 km to the northwest. The appearance of two low-V_p zones in the depth slice reflects minor relief on the surface of the single lower-V_p zone. Similarly, the V_s is anomalously low in the slightly tighter depth range of 9 to 11 km. We interpret the low-V_p and low-V_s regions to indicate the presence of rock containing about 4–6% geothermal brines [*Nakajima et al.*, 2001], although such interpretation is also dependent on the aspect ratios of the pore shapes [*Takei*, 2002]. The presence of very limited seismicity within this region is also consistent with the region being partially brittle.

[33] Relocated hypocenters within 3 km of each side of the cross sections are included to show relationships between velocity anomalies and the depth distribution of seismicity. Beneath the geothermal field, most of the seismicity that is located between 1- and 5-km depth is floored by a high-velocity lid between 4- to 6-km depth. Along the edges and just outside the geothermal field the base of seismicity abruptly increases to 10 to 12 km. Thus the depth distribution of the seismicity is consistent with the geometrical shape of the low-V_p and low-V_s anomalies and supports the interpretation that this region is anomalously hot and deforms mostly aseismically, with the brittle-ductile transition zone locally elevated to shallow depths above the low-velocity zone.

4.2. V_p/V_s and Poisson's Ratio Models

[34] The most prominent feature in the V_p/V_s cross section is the abrupt increase in V_p/V_s extending from the surface down to depth of 3 km beneath the Coso geothermal field (Figure 10). With minor exceptions, the variations in V_p/V_s at depths below 3 km have small amplitudes and limited spatial extent. At 10-km depth in both cross sections, there is a small body (about 1 km wide) of moderately elevated V_p/V_s beneath the Coso geothermal field.

[35] The depth distribution of the Poisson's ratio exhibits the same features as the V_p/V_s (Figure 10). The geothermal field is imaged as low Poisson's ratio (about 0.2 or less) extending from the surface to 2-km depth, suggesting predominance of quartz-rich granitic rocks [*Christensen*, 1996]. Similarly, within the geothermal area, *Lees and Wu* [2000] found Poisson's ratio of 0.224, lower than the crustal average of 0.25. They also found 2% average porosity; however, the porosity was locally as high as 12%.

[36] At 10-km depth beneath the geothermal field, there is a zone of elevated V_p/V_s and Poisson's ratio, which could be interpreted to indicate a 2 to 5% volume fraction of magma, based on the relations in the work of *Nakajima et al.* [2001].

Figure 9. Detailed views of the V_p and V_s models in the Coso area. (a) V_p cross section trending southwest ($A - A$'), (b) V_p cross section trending northwest ($B - B$'), (c) map view of the V_p model at 10-km depth and the location on the two cross sections, (d) V_s cross section trending southwest ($A - A$'), (e) V_p cross section trending northwest ($B - B$'), and (f) map view of the V_s model at 10-km depth and the location on the two cross sections. The DWS contour of 300 (white color) delineates parts of the models that are not resolved. Yellow curves are the 0.1 contour of the diagonal element of the resolution matrix. The hypocenters determined using the double-difference method within 5.0-km distance of the cross sections is also plotted. The location of the Coso geothermal area is indicated by the black star while the location of Red Hill volcano is indicated by a red star. ALFZ, Airport Lake fault zone; CHS, Coso Hot Springs; SNF, Sierra Nevada frontal fault; WHM, Wild Horse Mesa.

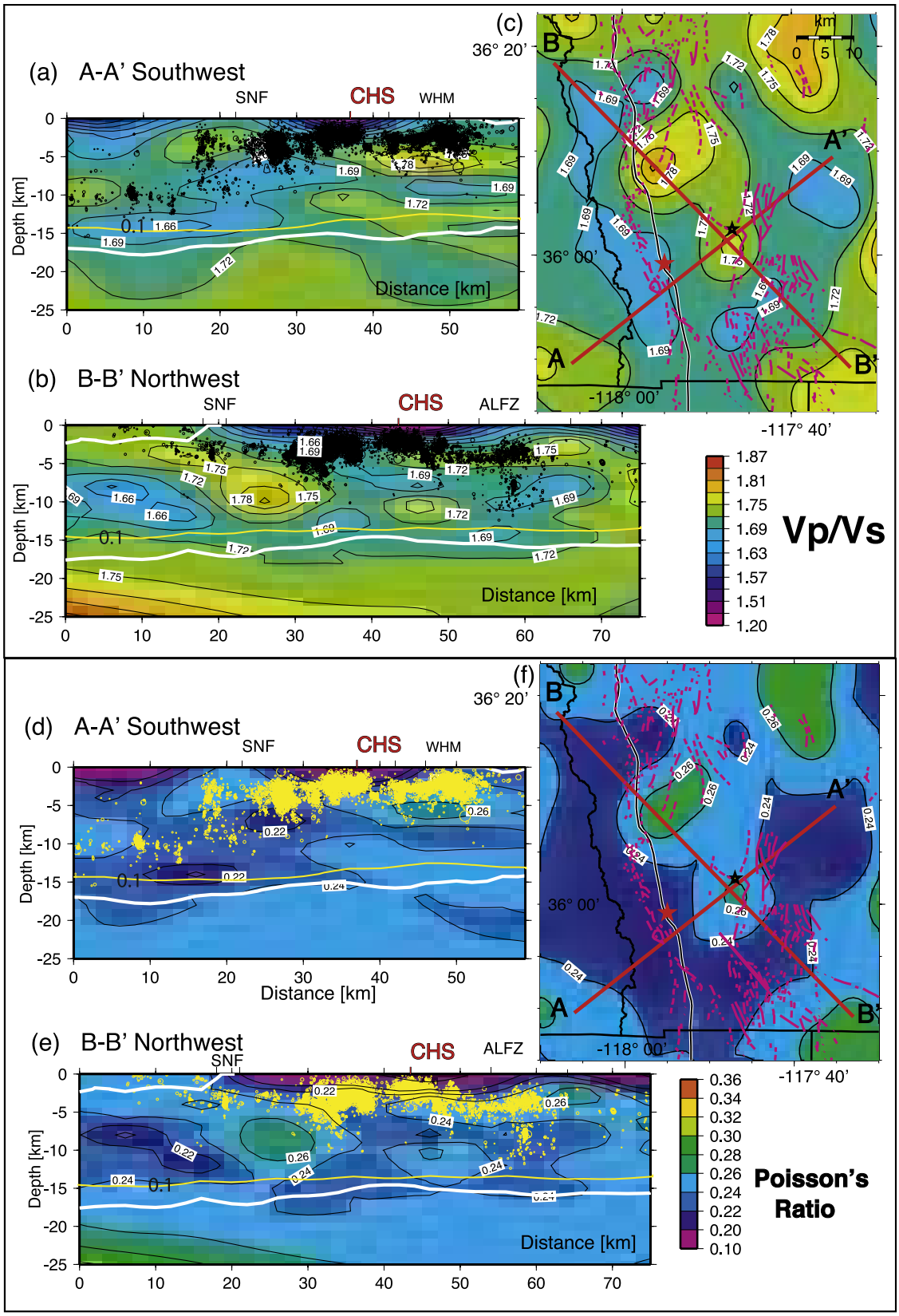
(a) A-A' Southwest
SNF
CHS
WHM
Depth [km]
Distance [km]
(b) B-B' Northwest
SNF
CHS
ALFZ
Depth [km]
Distance [km]
(c)
36° 20'
36° 00'
-118° 00'
-117° 40'
A
A'
B
B'
km
0 5 10
1.87
1.81
1.75
1.69
1.63
1.57
1.51
1.20
Vp/Vs
(d) A-A' Southwest
SNF
CHS
WHM
Depth [km]
Distance [km]
(e) B-B' Northwest
SNF
CHS
ALFZ
Depth [km]
Distance [km]
(f)
36° 20'
36° 00'
-118° 00'
-117° 40'
A
A'
B
B'
0.36
0.34
0.32
0.30
0.28
0.26
0.24
0.22
0.20
0.10
Poisson's Ratio

Figure 10

This anomalous zone is not resolved in the horizontal dimension but is well resolved in the vertical dimension, which has a 2-km grid spacing. The zone is only detected because it happens to be close to a grid node, although a spike test described in the Appendix showed that we would have detected a bigger V_p/V_s anomaly quite easily with our data set. Because of its spatial coincidence with the geothermal field and associated volcanics as well as other evidence provided by *Monestaro et al.* [2005], we cannot dismiss this anomaly out of hand. The small size of this anomaly is also consistent with the modest volume of erupted volcanics in the Pleistocene Coso volcanic field [*Manley and Bacon*, 2000].

[37] The absence of a broad high-V_p/V_s anomaly is in contrast to the results of *Wilson et al.* [2003], who used elevated V_p/V_s values to infer a much larger magma chamber below 5-km depth. One possibility is that the results of the work of *Wilson et al.* [2003] provide an image that is smeared in the vertical dimension because they use rays that are mostly vertical. Our method uses mostly horizontal rays and provides better vertical resolution. We interpret the anomalous zone at 10-km depth that may contain magma to be only about 1 km long and 1 km thick or possibly smaller or much smaller than advocated by *Wilson et al.* [2003] and *Monastero et al.* [2005]. Furthermore, the complete absence of seismicity in the depth range of the anomaly is consistent with the presence of anomalously high temperatures as compared to the region surrounding the Coso geothermal filed where seismicity extends at least to 12 km depth.

[38] Other regions of high or low V_p/V_s or Poisson's ratio, which are located at distance from Coso, are most simply interpreted as being associated with different rock formations rather than being associated with zones of elevated crustal temperatures and/or the presence of fluids. One such region is located to the northwest of Coso, beneath northern Rose Valley and the northwest Coso Range, where the cross-section $B - B$' indicates moderately elevated V_p/V_s and Poisson's ratio values, but almost no changes in V_p or anomalous V_s values (Figures 9 and 10). Because there is no V_p low or high heat flow anomaly in northern Rose Valley similar to that associated with the Coso geothermal field, we prefer to interpret the V_p/V_s anomaly beneath the northern Rose Valley as being caused by crustal compositional changes, with less quartz or silicate minerals and more mafic rocks. This region has a lower level of background seismicity compared to the Coso geothermal field, which also suggests different crustal composition and fluid content than in the Coso area.

4.3. Seismicity Patterns Near Coso

[39] To refine the hypocenters in the Coso region, we select only events within ~25-km distance of the Coso geothermal field, and add differential traveltimes determined using waveform cross correlation (study area II in Figure 1). We applied the double-difference algorithm [*Waldhauser and Ellsworth*, 2000] to relocate these earthquakes (Figure 11a). The progressive refinement in locations is exhibited through improved clustering, including the focusing of linear northwest or northeast trends. For instance, the spatial separation between the 1992 and 2001 swarms in Rose Valley is well resolved. The base of seismicity shallows from a regional depth of about ~11 to ~5 km beneath the central Coso Range, which we interpret as evidence for positive relief on the brittle-ductile transition zone beneath the geothermal field.

[40] The abundant Coso seismicity forms two major clusters, one extending to depths of ~5 km within a radius of ~4 km centered on the geothermal field and the second extending to depths of ~11 km in the distance range of ~8 to ~12 km from Coso (Figure 11a). The ~4-km-radius zone of seismicity may be controlled by fluid injection or withdrawal from the geothermal area, while seismogenic deformation at ~8- to ~12-km distance may be associated with the crustal anomalies in the ~10-km depth range, as well as the regional transtensional deformation associated with the northwest motion of the Sierran microplate.

[41] Small earthquake swarms occur frequently in the Coso region (Figure 11a). Within the geothermal area, there is induced seismicity by both fluid production and injection at shallow depth, as well as clusters of seismicity around the edges of the geothermal field. The possible mechanisms that may explain the concentration of seismicity around the geothermal area are thermal weakening and natural hydrofracturing [*Sibson and Rowland*, 2003]. The natural hydrofracturing could occur between lithostatically pressured sources of brines below 8-km depth and the hydrostatically pressured surface geothermal reservoir.

[42] The two largest earthquake swarms that occurred in April to May 1992 and May to June 2001 were located 5 to 8 km to the west of Coso. The Rose Valley swarm of April to June 1992 showed some spatial migration and doubled its spatial extent to 8 km within a few weeks, suggesting a fluid-migration-type driving force. The swarm of May to June 2001 showed similar behavior of spatial growth with time. The scattered seismicity within the Coso Range to the north consists mostly of small swarms and individual events.

[43] To the east of Coso, the more spatially and temporally scattered Wild Horse Mesa seismicity forms a north-northwest trend but coincides with a zone of numerous short north-northeast-striking faults [*Unruh et al.*, 2002]. The 1996 and 1998 earthquakes that occurred to the east of Coso exhibited faulting on conjugate fault planes striking northwest and northeast and caused changes in stress loading within the Coso geothermal field [*Bhattacharyya*

Figure 10. Detailed views of the V_p/V_s and Poisson's ratio models in the Coso area. (a) V_p/V_s cross section trending southwest ($A - A$'), (b) V_p/V_s cross section trending northwest ($B - B$'), (c) map view of the V_p model at 10-km depth and the location on the two cross sections, (d) Poisson's ratio cross section trending southwest ($A - A$'), (e) Poisson's ratio cross section trending northwest ($B - B$'), and (f) map view of the Possion's ratio model at 10-km depth and the location on the two cross sections. The DWS contour of 150 (white color) delineates parts of the model that are not resolved. Yellow curves are the 0.1 contour of the diagonal element of the resolution matrix. The hypocenters determined using the double-difference method within 5.0-km distance of the cross sections is also plotted. See also caption of Figure 9.

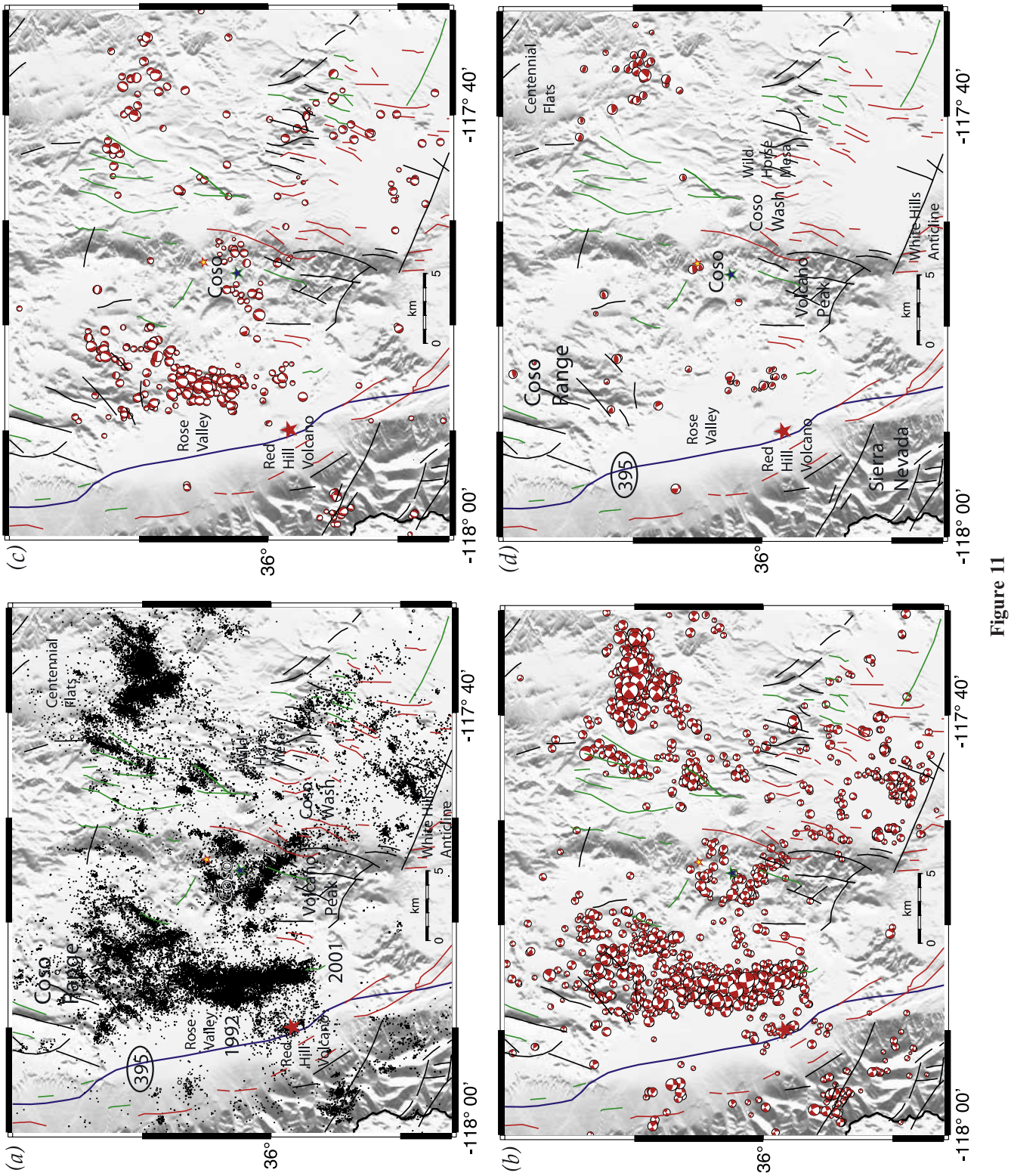
(a)
(b)
(c)
(d)
Coso Range
Centennial Flats
Rose Valley
Red Hill Volcano
Coso Volcanic Peak
Coso Wash
Wild Horse Mesa
White Hills Antidline
Sierra Nevada
395
1992
2001
36°
-118° 00'
-117° 40'
km
0
5

Figure 11

et al., 1999]. The temporal behavior of the Ridgecrest main shock-aftershock sequences of 1994 and the later Coso earthquake sequences of 1996 and 1998 suggests that the crustal stress loading process varies across the region because, in each case, the pairs of main shocks are spaced 47 days and 16 months apart, respectively.

4.4. Focal Mechanisms Patterns Near Coso

[44] The focal mechanisms of the relocated seismicity in the Coso region primarily exhibit right-lateral strike-slip faulting (~77%), as well as some normal (~21%) and limited thrust faulting (~2%) (Figures 11b, 11c, and 11d). The majority of the seismicity in the region, including the 1992 and 2001 Rose Valley swarms and the 1996–1998 Coso sequence exhibit predominantly strike-slip faulting on both northwest- and northeast-striking faults (Figure 11b). This strike-slip faulting regionally accommodates the northwest motion of the Sierran microplate with respect to stable North America [*Unruh et al.*, 2003].

[45] Some normal-faulting mechanisms with north- to north-northeast striking nodal planes also occur in the region, thus suggesting transtensional faulting (Figure 11c). These events are mostly spatially distributed among the strike-slip events, except above the V_p anomaly near Coso. Hence this subset of normal-faulting mechanisms identifies the locus of net crustal thinning in the central Coso Range, which occurs directly above the low-V_p anomaly [*Unruh et al.*, 2002]. The crustal thinning extends from Coso to the northwest as evidenced by normal-faulting events that occurred at the north end of the 2001 Rose Valley swarm. A few thrust-faulting events, with mostly east-west-striking planes, also have occurred in the region (Figure 11d). The thrust faulting is probably related to local geometrical complexities in the spatially complex strike-slip fault systems (for example, restraining bends and steps) and associated heterogeneity in the stress field.

4.5. Seismogenic Deformation Field Near Coso

[46] Using the new set of focal mechanisms prepared for this study, we inverted seismic P and T axes from discrete domains for components of a reduced incremental deformation tensor [*Twiss et al.*, 1993; *Unruh et al.*, 1997]. We used bootstrap methods to determine 95% confidence intervals for the parameters of the best fit models. The results of the inversions are plotted as the regional trends of the principal incremental strains d_1 (maximum extension) and d_3 (maximum shortening) in the study area (Figure 12). In general, both d_1 and d_3 are subhorizontal, consistent with regional northwest dextral shear associated with the northwest motion of the Sierran microplate. The incremental strain trajectories exhibit a clockwise rotation from east to west across the northern Coso Range. There is also a modest counterclockwise deflection of the trajectories through the geothermal production area.

[47] We also determined the values of the vertical component of the incremental strain tensor (V) to show local areas of significant or pronounced crustal thinning (Figure 13; see the work of *Unruh et al.* [2002] for the derivation and interpretation of V). Our results indicate that a northwest-southeast-trending region of transtensional deformation (i.e., $-0.8 < V < 0$), which includes components of both shearing and vertical crustal thinning, encompasses parts of Upper Cactus Flat, the main geothermal production area, and Coso Basin (Figure 13). However, most "transtensional" values of V ($-0.8 < V < 0$) cannot be statistically distinguished from a pure strike-slip style of deformation ($V = 0$) at the 95% confidence interval. Nonetheless, given the number and consistency of the negative values of V in this region, we believe that the extent and geometry of the "transtensional" region is generally correct, despite the large uncertainties in the inversion results.

[48] The area of net vertical thinning in the central Coso Range (Figure 13) is strongly correlated with the low-V_p anomaly beneath the geothermal field (Figure 14). The V_p and V lows ($V_p < 6$ km/s and $V < -0.5$, respectively) are generally coincident, and both are elliptical with their long axes subparallel and oriented northwest-southeast. This correlation suggests that the hot, ductile, and presumably less-viscous crust beneath the geothermal field is localizing transtension and brittle upper crustal thinning.

[49] Our new results also indicate that seismogenic deformation in the northern Indian Wells Valley and southern White Hills, which initially formed as a left-restraining anticline, is strongly transtensional to extensional. The results of the kinematic inversion are consistent with field observations that the Airport Lake fault zone breaks into multiple splays in this region, and northwest dextral slip generally is transferred in a releasing geometry to more northerly striking normal faults in southern Coso Wash, eastern Coso Basin, and southern Wild Horse Mesa. There is no indication in the seismicity of local crustal shortening associated with the short left-restraining steps across the White Hills anticline (Figure 12). However, the majority of seismicity in the White Hills is associated with vertical shear zones south of the White Hills anticline proper, not reverse faults beneath the forelimb of the fold.

5. Discussion

[50] This study has provided a new insight into the crustal structure and seismicity of the southern Sierra Nevada and the Coso Range as well as the transtensional nature of the Coso tectonics. The upper to middle crust appears to be rich in quartz, which is consistent with the granitic composition of Sierran batholiths. In contrast, there is almost no evidence for the presence of significant mafic crustal bodies.

Figure 11. The seismicity for 1981 to 2005 in central eastern California recorded by the Caltech/USGS Southern California Seismic Network and relocated using three-dimensional models and cross-correlation differential traveltimes input into the HypoDD code [*Waldhauser and Ellsworth*, 2000]. First-motion focal mechanisms of events in the general Coso area are also shown. (a) Waveform relocated 1981–2005 seismicity in the Coso area. The epicenters are shown as black circles scaled with magnitude, and the $M \geq 4.0$ earthquakes are shown as red stars. (b) Strike-slip focal mechanisms, (c) normal faulting, and (d) thrust faulting.

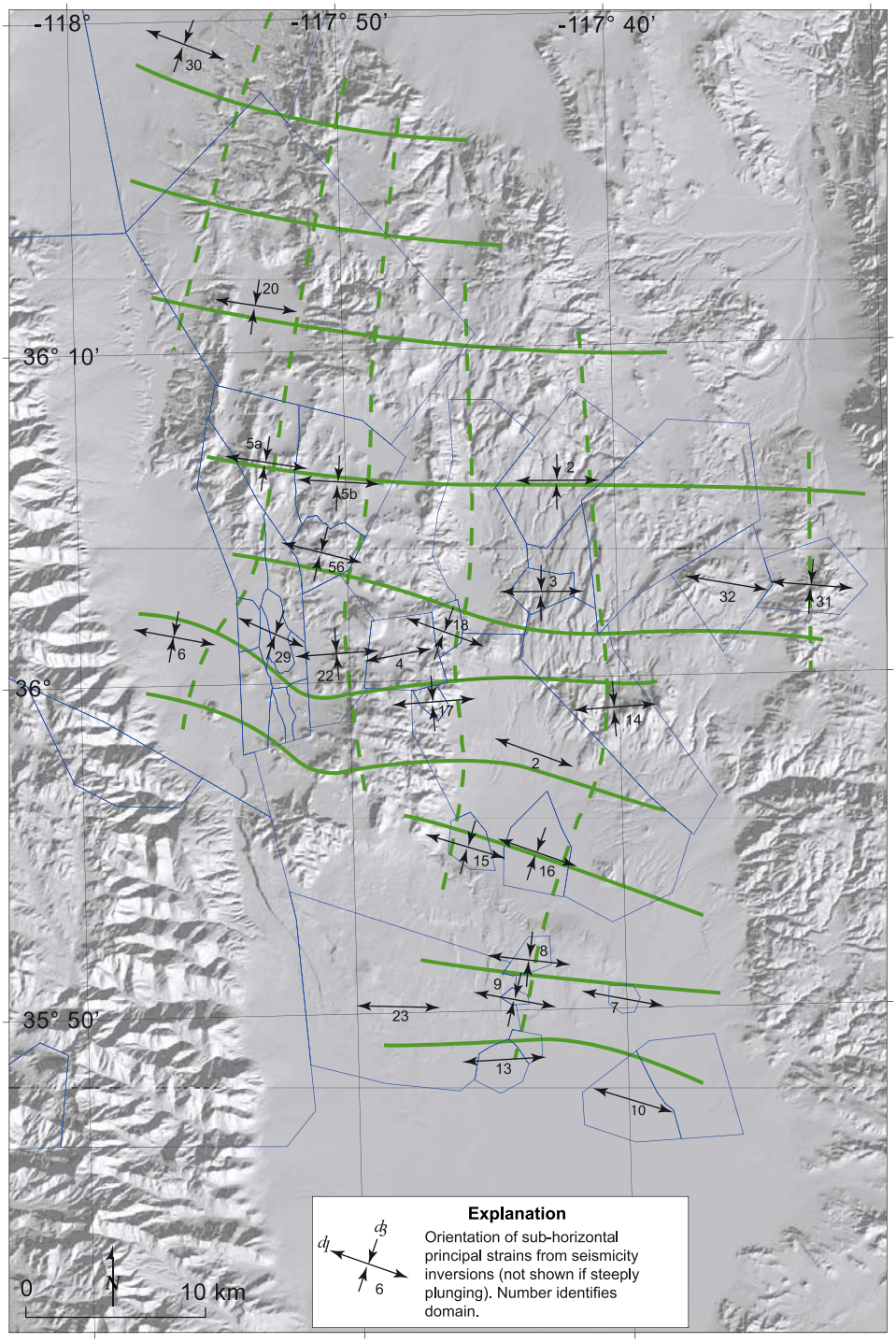

Figure 12. Horizontal trajectories of maximum extension (solid lines) and maximum shortening (dashed lines) from kinematic inversions of focal mechanisms. Seismic *P* and *T* axes from focal mechanisms within each polygon were grouped for the kinematic inversions; the paired arrows associated with each polygon provide the results of individual inversions.

5.1. Quartz-Dominated Crustal Composition

[51] The average three-dimensional velocities in the region are slightly lower than the average southern California crustal velocities with, for instance, the $V_p/V_s \sim 1.65$ to 1.7 in the near-surface and V_p of 6.3 km/s down at depths of 10 to 18 km. The moderately below average V_p, V_s, V_p/V_s, and Poisson's ratio values are consistent with the presence of granitic rocks as mapped in the southern Sierra and Coso Range [*Duffield and Bacon*, 1981] (Figure 6), which have low V_p/V_s and Poisson's ratio because of their high quartz content [*Christensen*, 1996]. Similarly, low V_p/V_s values are reported by *Brocher* [2005] for Salinian granites in central California.

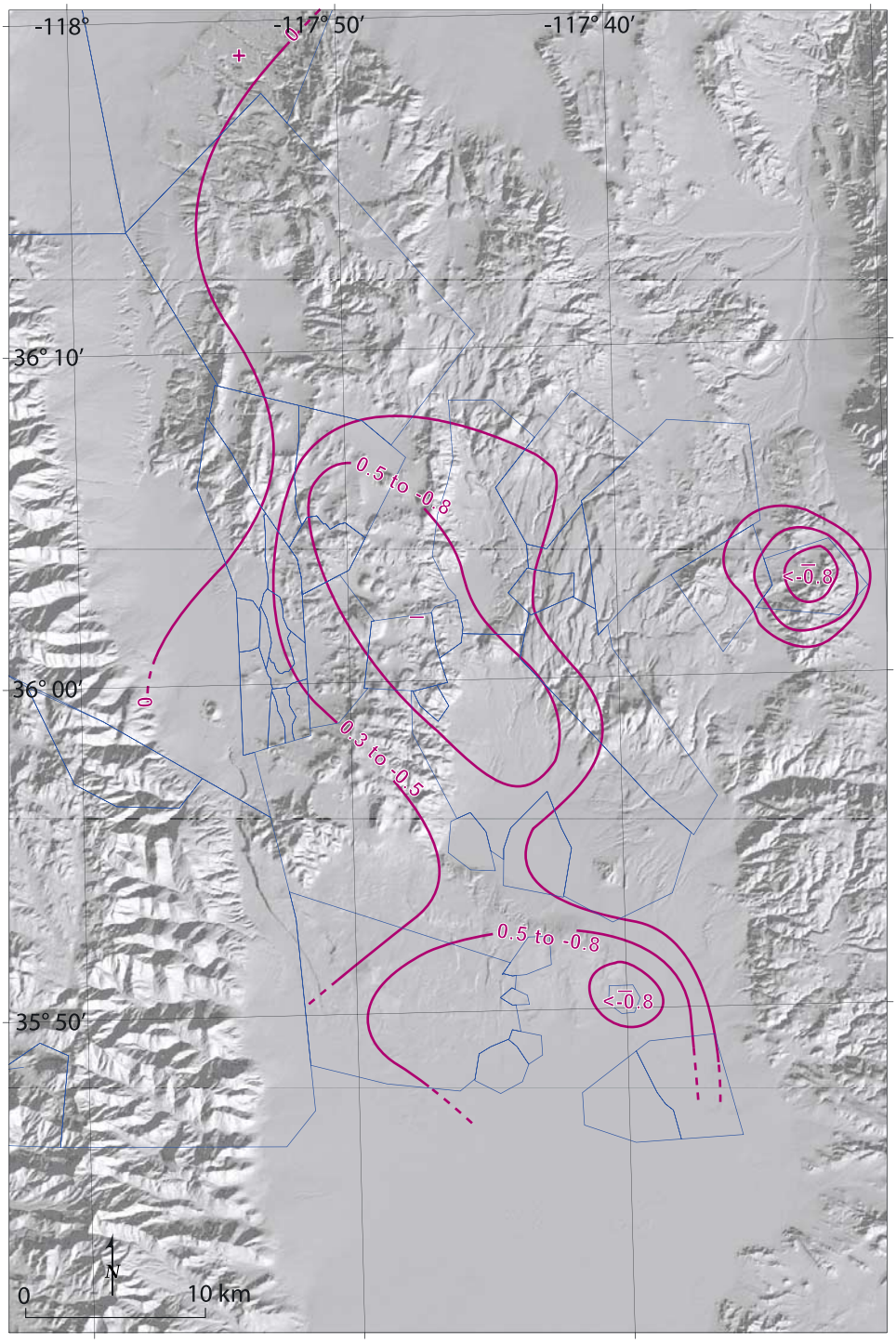

Figure 13. Contours of the vertical deformation parameter (V) derived from kinematic inversions of focal mechanisms. Negative values of V indicate net vertical crustal thinning and horizontal extension.

[52] The low V_p/V_s and Poisson's ratio for the Coso region agree with the results of *Lees and Wu* [2000] who found that the average Poisson's ratio in the depth range from the surface to 3 km is 0.22, which is below the crustal average of 0.25. They also found mostly low V_p/V_s in the near surface and concluded that the rocks are predominantly quartz-rich silicates. *Lees and Wu* [2000] were also able to resolve small zones, with dimensions on the order of 2 km, of higher V_p/V_s and Poisson's ratio, thus indicating larger crack density and more fluid flow. However, with 10-km horizontal grid spacing and similar or larger station spacing, we are not able to detect such small anomalies except when such anomalies happen to be located at a grid node.

[53] To understand the possible cause of the small-scale velocity heterogeneity at shallow depth, we have compared the V_p and V_p/V_s models with the regional three-dimensional

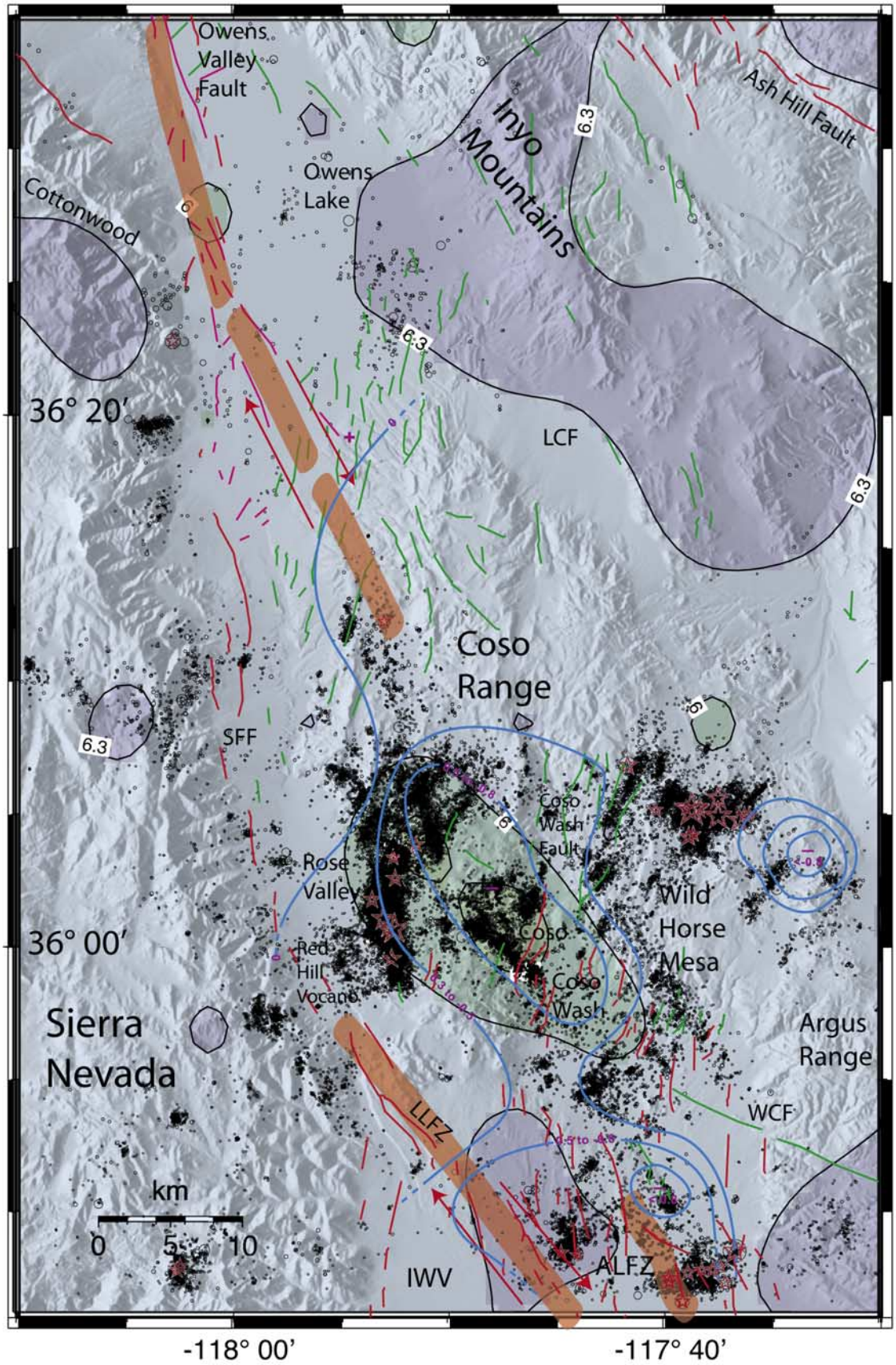
Owens
Valley
Fault
Owens
Lake
Cottonwood
Inyo
Mountains
Ash Hill Fault
6.3
36° 20′
LCF
Coso
Range
SFF
Coso
Wash
Fault
Rose
Valley
Wild
Horse
Mesa
36° 00′
Red
Hill
Volcano
Coso
Wash
Sierra
Nevada
Argus
Range
WCF
LLFZ
km
0 5 10
IWV
ALFZ
-118° 00′
-117° 40′

Figure 14

gravity model of the area by *Black et al.* [2002]. They found a northwest-trending structural fabric of alternating high and low gravity. These changes in gravity are approximately 2 to 5%, which corresponds to approximately 0.7 to 0.4% change in V_p or V_s velocities. For instance, 6.0 km/s would change by 0.02 to 0.04 km/s. These changes are too small to be detectable in our model, and thus it is not surprising that the variations in gravity as determined by *Black et al.* [2002] are not reflected in the V_p model. The shallow V_p/V_s model shows some faint hints of a northwest-trending regional grain with alternating high and low V_p/V_s values. This variation in V_p/V_s could be due to the gravity but are to small to be conclusively associated to northwest-trending dike swarms [*Black et al.*, 2002].

[54] Several other crustal velocity models that have been determined for the southern Sierra-Coso region also exhibit similar crustal velocities as found in this study. For instance, the west-to-east refraction profile of *Ruppert et al.* [1998], which extended across the Sierra Nevada, showed mostly 6.0 km/s upper crustal velocities with only minor spatial variations. The relative absence of crustal heterogeneity at midcrustal depths in the region is also consistent with the fairly constant depth to Moho of 30 to 32 km below sea level, as demonstrated in many studies, including *Jones and Phinney* [1998] and *Wilson et al.* [2003].

5.2. Imaging H_2O and Magma as Heat Sources Beneath Coso

[55] A magma chamber is commonly interpreted as being present beneath the Coso geothermal field at 5-km depth [e.g., *Wilson et al.*, 2003; *Monastero et al.*, 2005]. The results of our study do not agree with magma being at such a shallow depth, because we find pronounced low-V_p and low-V_s anomalies but almost no change in V_p/V_s above 10-km depth.

[56] To explain the geophysical, geochemical, and other anomalies beneath the Coso geothermal area, we favor a model that includes at least two different heat sources. The geothermal area that extends down to depths of ~5 km is probably floored by a narrow impermeable self-sealed zone of hydrothermally altered minerals, which approximately follows the brittle-ductile transition (BDT) as defined by the ~350°C geotherm [*Monastero et al.*, 2005]. The low-V_p, low-V_s, and almost normal V_p/V_s zone that is located beneath this self-healed zone is the first heat source. This zone is interpreted to primarily contain brines in the 6- to 11-km depth range, because the V_p/V_s and Poisson's ratio values are almost normal. This low-V_p anomaly is probably the same low-velocity zone imaged by previous workers and interpreted as a magma chamber [*Reasenberg et al.*, 1980; *Wilson et al.*, 2003].

[57] A similar model was suggested by *Fournier* [1999], who used petrological data to explain the formation of a lithostatically pressured zone at depth that includes hypersaline brine and gas exsolved from crystallizing magma. This lithostatically pressured zone is capped by a self-sealed brittle-ductile transition. When episodic breaches of the self-sealed brittle-ductile transition occur, temporary upsurge of fluids may increase the local strain rate and drive ductile rock to sustain brittle shear failure (and possibly expressed as seismicity swarms). Alternatively, transient increases in local strain rate may be sufficient to drive shear failure in rock that normally deforms via ductile flow at background tectonic rates in the region. For instance, the 1992 and 2001 Rose Valley swarm or the induced swarm activity related to the 1992 M_w7.3 Landers earthquake could have caused migration of fluids from the midcrustal brine reservoir to shallower depths, and in some cases into the actual Coso production zone.

[58] Our interpretation of the prominent V_p low-velocity anomaly and average V_p/V_s as being a zone of H_2O-rich, over-pressurized geothermal fluids is also supported independently by *Manley and Bacon* [2000] using evidence from melt inclusions. They provide examples of 6.2 wt% total H_2O melt inclusions that were saturated at lithostatic pressures, which were almost equivalent to 10 km of overburden. They also noted other examples of fluid inclusions from the depth range of 5 to 10 km. *Manley and Bacon* [2000] also concluded that the late Quaternary rhyolites erupted from a more shallow magma reservoir, about 4.5 km, than the older Quaternary volcanics thus inferring that the magma chamber had migrated upward with time. No such magma chambers above 10-km depth are imaged in our modeling, suggesting that they no longer exist or are too small to be detected.

[59] We propose that the primary heat source beneath Coso could be the small volume (<1 km^3) of low V_p and moderately elevated V_p/V_s at ~10-km depth. This anomalous volume is so small that it is at the lower limit of the horizontal resolution but within the vertical resolution of our model and is only detected because it happens to be near a node in the model. Under normal circumstances we would ignore this small anomaly, but its coincidence with the broader V_p anomaly and being located beneath the geothermal area, a region of late Quaternary volcanism, provides circumstantial evidence for our interpretation. We speculate that this anomalous volume may be related to the upward migration of successively shallower rhyolitic magma chambers of small diameter (<1 km), as suggested by *Manley and Bacon* [2000]. They analyzed the mineral composition and determined the thermobarometry for minerals in rhyolites within the Coso area and found 39 high-silica rhyolite domes and lava flows that were erupted from both 10- and 5-km depth. The younger rhyolites came from a shallower depth. *Manley and Bacon* [2000] estimated the total volume of erupted rhyolite of ~1.6 km^3 flanked on three sides by monogenetic basaltic volcanoes, which is

Figure 14. Schematic view of transtensional tectonics of the Coso region. Extensional faulting within the Coso Range occurs in a releasing right step over between the Owens Lake fault to the north and the Airport Lake fault zone to the south. The low-V_p anomaly beneath the central Coso Range coincides with the releasing step and locus of transtensional crustal thinning, which are shown as (blue) contours of the vertical deformation parameter (from Figure 13). Superimposed on the background topography is the three-dimensional V_p model at 10-km depth, relocated seismicity and mapped faults. Red, Holocene; green, late Quaternary. ALF, Airport Lake fault zone; IWV, Indian Wells Valley; LLFZ, Little Lake fault zone; SFF, Sierran frontal fault; WCF, Wilson Canyon fault; LCF, Lower Centennial Flats.

consistent with the small size of this low-V_p and moderately higher V_p/V_s volume.

[60] In detail, our results differ from those of *Wilson et al.* [2003], who used mostly vertical rays from teleseisms in their analysis and reported much higher V_p/V_s ratios of 2.5 at 5-km depth. They interpreted the high V_p/V_s being caused by the presence of magma at 5 km or greater depth. They applied the relationships between V_p/V_s, V_p, and crack aspect ratios of *Nakajima et al.* [2001] to infer 1.5 to 5 vol% of melt below 5-km depth, in a region of at least 125 km^3, which if present would be easily detected by our technique, see also Appendix. In contrast, we observed ~10% reduction in V_p and $V_p/V_s \sim 1.72$, which per *Nakajima et al.* [2001] can only be caused by the presence of ~1 vol% of H_2O with a crack aspect ratio of ~1:100, or about 2.5 times larger than the crack aspect ratio of 1:38 for the Coso geothermal field determined by *Lees and Wu* [1999].

5.3. Regional Extensional Tectonics

[61] The Coso Range is interpreted as a zone of distributed extension in a releasing step over between northwest-striking dextral faults such as the Little Lake and Airport Lake fault zones to the south and the Owens Valley fault to the north [e.g., *Walter and Weaver*, 1980]. This interpretation is preferred in part because it is not possible to identify a single throughgoing major fault that transfers slip through the central Coso Range between the Owens Valley fault and Airport Lake fault zone [*Unruh et al.*, 2002]. Furthermore, the seismicity is scattered, and the late Quaternary fault patterns in the Coso Range are complex [*Bacon et al.*, 1980; *Jennings*, 1994].

[62] Synthesis of the relocated seismicity, mapped faults from the work of *Jennings* [1994], localized crustal thinning, and the V_p model at 10-km depth illustrates how and where the step over of crustal deformation may be accommodated (Figure 14). The V_p anomaly at 10-km depth is elongated northwest-southeast, subparallel to the direction of regional dextral shear determined for the focal mechanisms. It also coincides with the area of transtensional crustal thinning, as determined from the kinematic analysis of focal mechanisms. Seismicity appears to overlap the main V_p anomaly to the west, but is largely absent on the east and northeast flanks of the anomaly in the Wild Horse Mesa region. Thus the step over appears to be a 20-km broad zone that is centered on the area of the V_p anomaly.

[63] Within the step over, numerous short seismogenic faults strike northwest, dip northeast, and accommodate dextral-oblique normal displacement. As an example, the Wild Horse Mesa area that is moving obliquely to the southeast relative to the Sierra Nevada as part of the Walker Lane belt is being deformed by both strike-slip and normal faulting. In the vicinity of the geothermal area, this faulting is exceptionally shallow. The elevated brittle-ductile transition zone suggests that ductile flow in the upper middle crust may be an additional mechanism for accommodating the transfer of the dextral slip.

6. Conclusions

[64] Only minor changes in the crustal velocity structure occur across the Sierran frontal fault, characterized by midcrustal V_p of 6.0 km/s being ~2 km shallower under the Sierra Nevada than to the east beneath the Coso-Ridgecrest area. To the east of the Sierran frontal fault, prominent low-V_p and low-V_s crustal anomalies are imaged beneath the central Coso Range. These anomalies are elongated northwest and southeast in the depth range of 8 to 12 km. We interpret the presence of low V_p and absence of very high V_p/V_s values at midcrustal depths to indicate the presence of superheated brines (H_2O) underlain by possibly a few percent volume fraction of melt at depth of ~10 km. The brittle-ductile transition zone, as defined by maximum depth of seismicity, is locally elevated from a regional depth of about 11 km to as shallow as about 5 km over the low-V_p and low-V_s crustal anomaly beneath the Coso geothermal field. However, the presence of some seismicity within this region is also consistent with the region being capable of brittle deformation. At ~10-km depth, there is a zone of anomalously low V_p and slightly elevated V_p/V_s, which could be inferred as 2 to 5% fraction of the volume of magma, using the relations in the work of *Nakajima et al.* [2001]. This zone could be a tabular, sill-like body that is about 2 km long and 1 km thick or possibly smaller. Furthermore, the virtual absence of seismicity in this deeper depth range is consistent with the presence of high temperatures and possibly magma. The small size of this deep anomaly is also consistent with the small diameter of ~4 km of the geothermal field and the limited volume of erupted material in the Pleistocene Coso volcanic field. The seismicity shows swarm-like behavior, possibly due to fluid migration or triggering by distant earthquakes. The area of net vertical thinning in the central Coso Range, as determined from the kinematic analysis of focal mechanisms, is strongly correlated with the low-V_p anomaly beneath the geothermal field. Active strike-slip and normal faults that transfer NW dextral shear strain from the Airport Lake fault zone to the Owens Valley fault zone across the Coso Range are located within or along the edges of the crustal anomalies.

Appendix A

A1. Three-Dimensional V_p and V_p/V_s Model Quality

[65] The errors in the final three-dimensional V_p and V_p/V_s models are caused by factors such as errors in the traveltimes, uneven ray coverage, ray-tracing methods, as well as possibly incorrect parameterization or starting velocity model. We have calculated the resolution matrix, the derivative weighted sum, and the standard error to evaluate effects of traveltime errors, and uneven ray coverage. We investigated the effects of choice of starting model and parameterization and possible nonlinearity by testing different grids, starting models, and damping parameters. To evaluate the effects of data errors, ray-tracing method, and uneven ray coverage, we calculated the resolution matrix, the derivative weighted sum, and the standard error.

[66] We calculate the model resolution matrix R for the damped least squares problem as [*Menke*, 1998],

$$R = \left(M^T M + L\right)^{-1} M^T M \tag{A1}$$

where M is the matrix of partial derivatives. If the resolution is perfect and the diagonal elements of the damping matrix

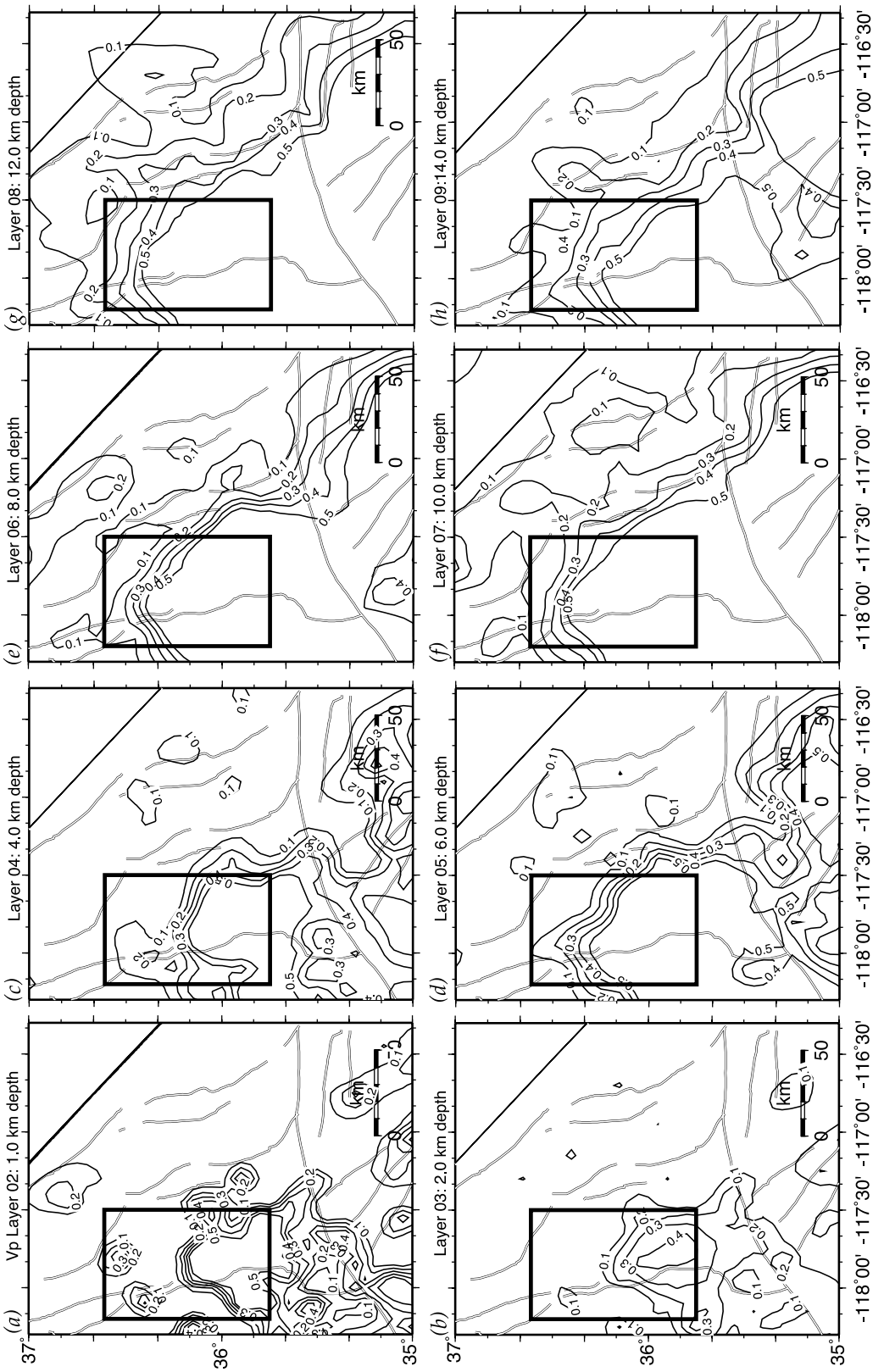

Figure A1. Diagonal elements of the resolution matrix for the final three-dimensional V_p model shown in depth slices at (a) 1-, (b) 2-, (c) 4-, (d) 6-, (e) 8-, (f) 10-, (g) 12-, and (h) 14.0-km depth. The model is well resolved within the contour lines.

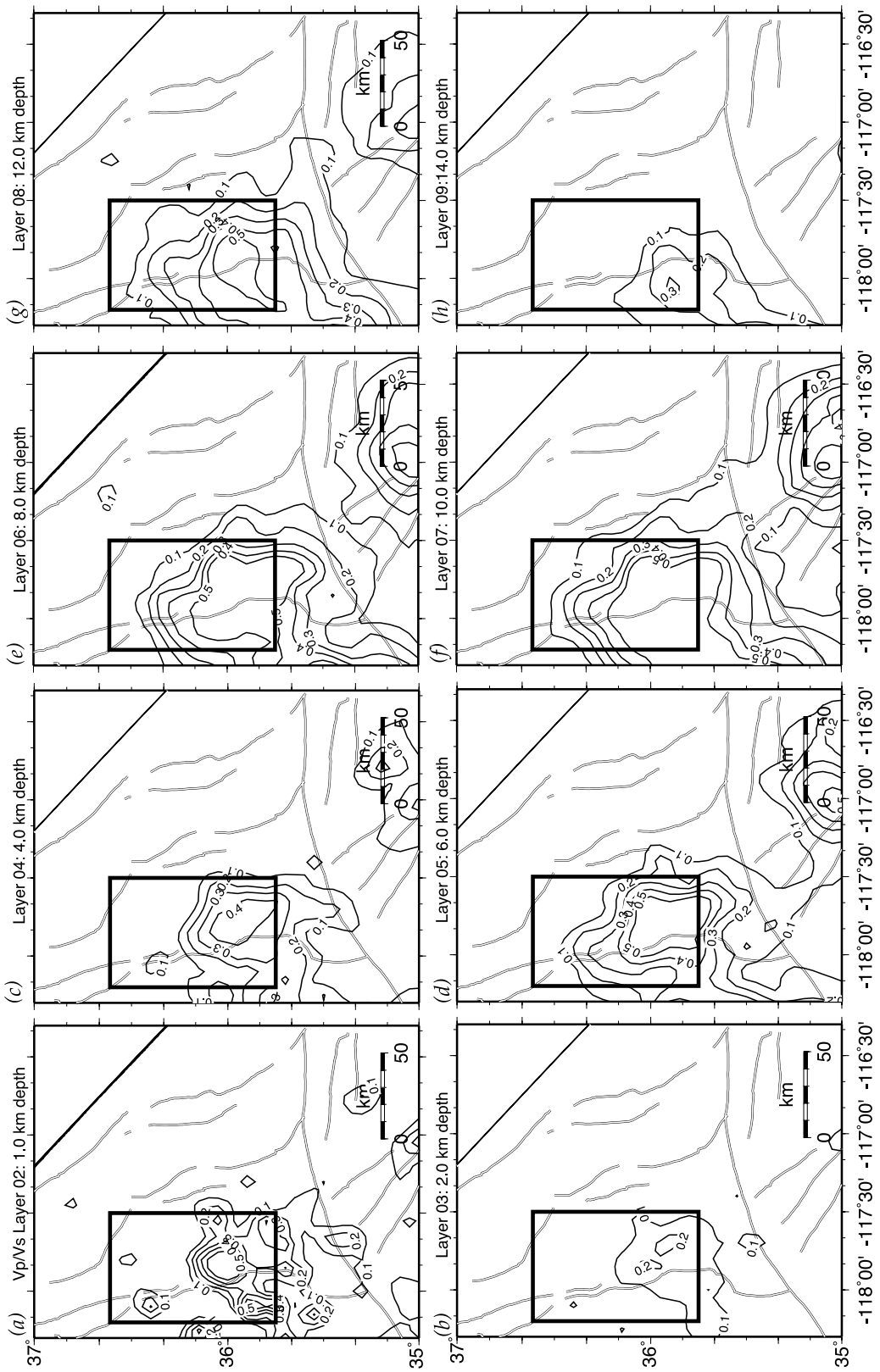

Figure A2. Diagonal elements of the resolution matrix for the final three-dimensional V_p/V_s model.

L are all zero, the model resolution is the identity matrix. Using damping, we determine the values of the diagonal elements of the resolution matrix that range from 0 to 1.0, where 0 is unresolved and 1.0 is completely resolved. We did not save the full resolution matrix because it exceeds 1 Gb in size and does not add new information about the resolution of the model.

[67] The central parts of the V_p and V_p/V_s models are well resolved, whereas the north and east edges show low values for the diagonal element of the resolution matrix and hence low resolution (Figures A1 and A2). The spatial distribution of the V_p and V_p/V_s anomalies appears to be real because there are no obvious correlations between the poorly resolved regions and the anomalies in the final models (Figures 6 and 7).

[68] We calculated the model standard error to determine an estimate of the mapping of the data error into the model error. The standard error calculated from the covariance matrix is small and varies throughout the model with errors in V_p ranging from 0.01 to 0.03 km/s. The calculated V_p/V_s standard errors range from 0.01 to 0.03. *Thurber* [1983], using the same SIMULPS approach for velocity inversions, suggested that, to obtain realistic standard error estimates, the calculated standard error should be multiplied a factor of 2. If we multiply with a factor of 2, the standard error remains small but would be similar to estimates in other studies.

[69] The derivative weighted sum (DWS) of the nth velocity parameter is defined as

$$\mathrm{DWS}(V_n) = N \sum_i \sum_j \left\{ \int_{P_{ij}} \omega_n(x) \mathrm{d}s \right\} \qquad \text{(A2)}$$

where i and j are the indices for event and station, ω is the linear interpolation weight that depends on coordinate position, P_{ij} is the raypath from i to j, and N is the normalization for the volume influenced by V_n [*Toomey and Fougler*, 1989].

[70] We use the DWS as a measure of the information density provided by the ray coverage (for additional detail, see also *Hauksson* [2000]). In general, the DWS values show that the three-dimensional V_p and V_p/V_s models are well resolved at depths from 2 to 14 km, while the near-surface layer and the bottom layers are less well resolved (Figures 6 and 7).

A2. Spike Tests

[71] To test for possible contamination between the V_p and V_p/V_s models we carried out the following test. The 10-km-depth layer of the starting V_p model has a uniform V_p of 6.25 km/s. First, we added a negative spike of 5.65 km/s into the 10-km-depth layer at the location of the V_p anomaly. Second, we calculated synthetic traveltimes for our specific data set through this model. Third, we used the synthetic traveltimes to invert for a three-dimensional model. We recovered 72% of the initial anomaly, or a V_p of 5.82 km/s. The lower value is to be expected from the damped inversion. The V_p/V_s ratio was 1% higher at this same grid point. We conclude that potential leakage from the V_p model into the V_s or V_p/V_s models is only on the order of 1% and thus insignificant for our results, although *Wagner et al.* [2005] found somewhat higher leakage in a different experiment.

[72] To test our ability to resolve a larger V_p/V_s anomaly at 10 km and at the location of the V_p anomaly, we performed a similar test using the starting V_p/V_s model with an unfirm V_p/V_s of 1.73. We added a positive spike (V_p/V_s = 1.83) into the 10-km-depth layer of V_p/V_s model at the location of the magma chamber and calculated synthetic traveltimes. We then inverted the synthetic traveltimes and recovered 99% of the spike or V_p/V_s of 1.81. From this test and the values of the diagonal element of the resolution matrix, we conclude that, if a large V_p/V_s anomaly was present beneath Coso, it would be easily detected by our method and data set.

[73] To improve our understanding of how well the small V_p/V_s anomaly at 10-km depth is resolved, we regridded the final 10-km horizontal grid model into 1.0-km horizontal grid. We recalculated the model using this denser grid and traveltimes traced through the 10-km model. The V_p/V_s anomaly remains at the same position in the model with a radius of about 1 km. Thus, although the V_p/V_s anomaly is poorly resolved, it is a stable feature in the models.

[74] **Acknowledgments.** This study was funded by the US Navy Geothermal Program Office (contract number N68936-02-C-0207) as well as U.S. Geological Survey Grants 05HQGR0040, 06HQGR0052, and 07HQGR0048 to Caltech. We thank the JGR reviewers and the associate editor for constructive reviews. Most figures were done using GMT [*Wessel and Smith*, 1991]. Contribution 9154, Division of Geological and Planetary Sciences, California Institute of Technology, Pasadena.

References

Argus, D. F., and R. G. Gordon (1991), Current Sierra Nevada-North America motion from very long baseline interferometry: Implications for the kinematics of the western United States, *Geology*, *191*, 1085–1088.

Bacon, C. R., W. A. Duffield, and K. Nakamura (1980), Distribution of Quaternary rhyolite domes of the Coso Range, California: Implications for extent of the geothermal anomaly, *J. Geophys. Res.*, *85*, 2425–2433.

Bawden, G. W., A. J. Michael, and L. H. Kellogg (1999), Birth of a fault: Connecting the Kern County and Walker Pass, California earthquakes, *Geology*, *27*, 601–604.

Bhattacharyya, J., S. Gross, J. Lees, and M. Hastings (1999), Recent earthquake sequences at Coso: Evidence for conjugate faulting and stress loading near a geothermal field, *Bull. Seismol. Soc. Am.*, *89*(3), 785–795.

Black, R. A., J. D. Walker, and G. S. Baker (2002), Three-dimensional gravity modeling and crustal-density variations, Panamint Range to the eastern Sierra Nevada, southeastern California, *Mem. Geol. Soc. Am.*, *105*, 229–241.

Brocher, T. M. (2005), Empirical relations between elastic wave speeds and density in the Earth's crust, *Bull. Seism. Soc. Am.*, *95*, 2081–2092, doi:10.1785/0120050077.

Christensen, N. I. (1996), Poisson's ratio and crustal seismology, *J. Geophys. Res.*, *101*, 3139–3156.

Duffield, W. A., and C. R. Bacon (1981), Geologic map of the Coso Volcanic field and adjacent areas, U.S. Geological Survey Miscellaneous Investigations Series Map I-1200, Inyo County, California, scale 1:50,000.

Feng, Q., and J. M. Lees (1998), Microseismicity, stress, and fracture in the Coso geothermal field, California, *Tectonophysics*, *289*, 221–238.

Fournier, R. O. (1999), Hydrothermal processes related to movement of fluid from plastic into brittle rock in the magmatic-epithermal environment, *Econ. Geol.*, *94*, 1193–1212.

Hardebeck, J. L., and P. M. Shearer (2002), A new method for determining first-motion focal mechanisms, *Bull. Seismol. Soc. Am.*, *92*, 2264–2276.

Hauksson, E. (2000), Crustal structure and seismicity distribution adjacent to the Pacific and North America plate boundary in southern California, *J. Geophys. Res.*, *105*, 13,875–13,903.

Hauksson, E., and P. Shearer (2005), Southern California hypocenter relocation with waveform cross-correlation: Part 1. Results using the double-difference method, *Bull. Seismol. Soc. Am.*, *95*, 896–903.

Hauksson, E., K. Hutton, H. Kanamori, L. Jones, J. Mori, S. Hough, and G. Roquemore (1995), Preliminary report on the 1995 Ridgecrest earthquake sequence in eastern California, *Seismol. Res. Lett.*, *66*(no. 6), 54–60.

Jennings, C. W. (1994), Fault activity map of California and adjacent areas: California Department of Conservation, Division of Mines and Geology, Geologic Data Map No. 6, scale 1:750,000.

Jones, C. H., and R. A. Phinney (1998), Seismic structure of the lithosphere from teleseismic converted arrivals observed at small arrays in the southern Sierra Nevada and vicinity, California, *J. Geophys. Res.*, *103*, 10,065–10,090.

Lees, J. M. (2002), Three-dimensional anatomy of a geothermal field, Coso, southeast-central California, *Mem. Geol. Soc. Am.*, *195*, 259–276.

Lees, J. M., and H. Wu (1999), P-wave anisotropy, stress, and crack distribution at Coso geothermal field, California, *J. Geophys. Res.*, *104*, 17,955–17,973.

Lees, J. M., and H. Wu (2000), Poisson's ratio and porosity at Coso geothermal area, California, *J. Volcanol. Geotherm. Res.*, *95*, 157–173.

Manley, C. R., and C. R. Bacon (2000), Rhyolite thermobarometry and the shallowing of the magma reservoir, Coso volcanic field, *J. Petrol.*, *41*, 149–174.

McClusky, S. C., S. C. Bjornstad, B. H. Hager, R. W. King, B. J. Meade, M. M. Miller, F. C. Monastero, and B. J. Souter (2001), Present day kinematics of the eastern California shear zone from a geodetically constrained block model, *Geophys. Res. Lett.*, *28*, 3369–3372, doi: 10.1029/2001GL0130912001.

Menke, W. (1998), *Geophysical Data Analysis: Discrete Inverse Theory,* Univ. of Calif. Press, Berkeley.

Monastero, F. C., J. D. Walker, A. M. Katzenstein, and A. E. Sabin (2002), Neogene evolution of the Indian Wells Valley, east-central California, in Geologic Evolution of the Mojave Desert and Southwestern Basin and Range, edited by A. F. Glazner, J. D. Walker, and J. M. Bartley, Boulder, Colorado, Geol. Soc. Am. Memoir, 195, 199–228.

Monastero, F. C., A. M. Katzenstein, J. S. Miller, J. R. Unruh, M. C. Adams, and K. Richards-Dinger (2005), The Coso geothermal field: A nascent metamorphic core complex, *Geol. Soc. Am. Bull.*, *117*, 1534–1553, doi:10.1130/B25600.1.

Nakajima, J., T. Matsuzawa, A. Hasegawa, and D. Zhao (2001), Three-dimensional structure of V_p, and V_s, and V_p/V_s beneath northeastern Japan: Implications for arc magmatism and fluids, *J. Geophys. Res.*, *106*, 21,843–21,857.

Reasenberg, P., W. Ellsworth, and A. Walter (1980), Teleseismic evidence for a low-velocity body under the Coso geothermal resource area, *J. Geophys. Res.*, *85*, 2471–2483.

Roquemore, G. (1980), Structure, tectonics and stress field of the Coso Range, Inyo County, California, *J. Geophys. Res.*, *85*, 2434–2440.

Roquemore, G., and J. Zellmer (1983), Ground cracking associated with the 1982 Magnitude 5.2 Indian Wells Valley earthquake, California, *Geology*, *36*, 197–200.

Ruppert, S., M. M. Fliedner, and G. Zandt (1998), Thin crust and active upper mantle beneath the Southern Sierra Nevada in the western United States, *Tectonophysics*, *286*, 237–252.

Sibson, R. H., and J. V. Rowland (2003), Stress, fluid pressure and structural permeability in seismogenic crust, North Island, New Zealand, *Geophys. J. Int.*, *154*, 584–594.

Takei, Y. (2002), Effect of pore geometry on V_p/V_s: From equilibrium geometry to crack, *J. Geophys. Res.*, *107*(B2), 2043, doi:10.1029/2001JB000522.

Thurber, C. H. (1983), Earthquake locations and three-dimensional crustal structure in the Coyote Lake area, central California, *J. Geophys. Res.*, *88*, 8226–8236.

Thurber, C. H. (1993), Local earthquake tomography: Velocities and V_p/V_s—Theory, in *Seismic Tomography: Theory and Practice*, edited by H. M. Iyer and K. Hirahara, pp. 563–583, CRC, Boca Raton, Fla.

Toomey, D. R., and G. R. Foulger (1989), Tomographic inversion of local earthquake data from the Hengill-Grensdalur central volcano complex, Iceland, *J. Geophys. Res.*, *94*, 17,497–17,510.

Twiss, R. J., B. J. Souter, and J. R. Unruh (1993), The effect of block rotations on the global seismic moment tensor and patterns of seismic P and T axes, *J. Geophys. Res.*, *98*, 645–674.

Unruh, J. R., R. J. Twiss, and E. Hauksson (1997), Kinematics of post-seismic relaxation from aftershocks of the 1994 Northridge, California earthquake, *J. Geophys Res.*, *102*, 24,589–24,603.

Unruh, J. R., E. Hauksson, F. C. Monastero, R. J. Twiss, and J. C. Lewis (2002), Seismotectonics of the Coso Range-Indian Wells Valley region, California: Transtensional deformation along the southeastern margin of the Sierran microplate, in Geologic Evolution of the Mojave Desert and Southwestern Basin and Range, edited by A. F. Glazner, J. D. Walker, and J. M. Bartley, Boulder, Colorado, Geol. Soc. Am. Memoir, 195, 277–294.

Unruh, J., J. Humphrey, and A. Barron (2003), Transtensional model for the Sierra Nevada frontal fault system, eastern California, *Geology*, *31*, 327–330.

Unruh, J., and E. Hauksson, (2007), Seismotectonics of an evolving intra-continental plate boundary, eastern California, *in review for* GSA special publication on the walker lane belt.

Wagner, L. S., S. Beck, and G. Zandt (2005), Upper mantle structure in the south central Chilean subduction zone (30° to 36°S), *J. Geophys. Res.*, *110*, B01308, doi:10.1029/2004JB003238.

Walck, M. C. (1988), Three-dimensional V_p/V_s variations for the Coso region, California, *J. Geophys. Res.*, *93*, 2047–2052.

Walck, M. C., and R. W. Clayton (1987), P wave velocity variations in the Coso region, California, derived from local earthquake travel times, *J. Geophys. Res.*, *92*, 393–405.

Waldhauser, F., and W. L. Ellsworth (2000), A double-difference earthquake location algorithm: Method and application to the northern Hayward Fault, California, *Bull. Seismol. Soc. Am.*, *90*, 1353–1368.

Walker, J. D., M. W. Martin, and A. F. Glazner (2002), Late Paleozoic to Mesozoic development of the Mojave Desert and environs, California, in Geologic Evolution of the Mojave Desert and Southwestern Basin and Range, edited by A. F. Glazner, J. D. Walker, and J. M. Bartley, Boulder, Colorado, Geol. Soc. Am. Memoir, 195, 1–18.

Walsh, J. B. (1965), The effect of cracks in rocks on Poisson's ratio, *J. Geophys. Res.*, *70*, 5249–5257.

Walter, A. W., and C. S. Weaver (1980), Seismicity of the Coso Range, California, *J. Geophys. Res.*, *85*, 2441–2458.

Wessel, P., and W. H. F. Smith (1991), Free software helps map and display data, *Eos Trans. AGU*, *72*, 441, 445–446.

Wicks, C. W., W. Thatcher, F. C. Monastero, and M. A. Hasting (2001), Steady state deformation of the Coso Range, east central California, inferred from satellite radar interferometry, *J. Geophys. Res.*, *106*(B7), 13,769–13,780, doi:10.1029/2001JB000298.

Wilson, C. K., C. H. Jones, and H. J. Gilbert (2003), Single-chamber silicic magma system inferred from shear wave discontinuities of the crust and uppermost mantle, Coso geothermal area, California, *J. Geophys. Res.*, *108*(B5), 2226, doi:10.1029/2002JB001798.

Wu, H., and J. M. Lees (1999), Three-dimensional P and S wave velocity structures of the Coso geothermal area, California, from microseismic traveltime data, *J. Geophys. Res.*, *104*, 13,217–13,233.

E. Hauksson, Seismological Laboratory, Division of Geological and Planetary Sciences, California Institute of Technology, Pasadena, CA 91125, USA. (hauksson@gps.caltech.edu)

J. Unruh, William Lettis & Assoc., 1777 Botelho Dr., Suite 262, Walnut Creek, CA 94596, USA. (unruh@lettis.com)